V.Yu. Sergeev, O.A. Bakhareva, A.I. Kislyakov, A.Yu. Kostrukov, B.V. Kuteev,
M.P. Petrov, V.G. Skokov, R. Burhenn, M. Kick

Conceptual design of Pellet Charge eXchange (PCX)

diagnostics for stellarator W7-X

V.Yu. Sergeev, O.A. Bakhareva, A.I. Kislyakov, A.Yu. Kostrukov, B.V. Kuteev,
M.P. Petrov, V.G. Skokov, R. Burhenn, M. Kick

Conceptual design of Pellet Charge eXchange (PCX)

diagnostics for stellarator W7-X

Conceptual design of Pellet Charge eXchange (PCX) diagnostics for stellarator W7-X

Y.Yu Sergeev, B.V. Kuteev, O.A. Bakhareva, A.Yu. Kostrukov, V.G. Skokov
State Technical University, St. Petersburg, Russia

M.P. Petrov, A.I. Kislyakov
Ioffe Physical Technical Institute, St. Petersburg, Russia

R. Burhenn, M. Kick
Max-Planck-Institut für Plasmaphysik, EURATOM Ass.
85748 Garching

Conceptual design of Pellet Charge eXchange (PCX) diagnostics for stellarator W7-X

V.Yu. Sergeev, B.V. Kuteev, O.A. Bakhareva, A. Yu. Kostrukov, V.G. Skokov

State Technical University, St. Petersburg, Russia

M.P. Petrov, A.I. Kislyakov

Ioffe Physical Technical Institute, St. Petersburg, Russia

R. Burhenn, M. Kick

Max-Planck-Institut für Plasmaphysik, Garching, Germany

Abstract

Pellet Charge eXchange diagnostic using Li pellets has been considered for the W7-X machine. Geometry of the experimental set-up and parameters of both Lithium Pellet Injector (LPI) and Neutral Particle Analyser (NPA) were evaluated. It was shown that this diagnostics can provide very well detectable H^0 signal in the range $50 - 1000$ keV generated by RF driven H^+ minority ions in W7-X. The PCX diagnostics will be able to measure H^+ energy spectra and density profiles in wide range of W7-X plasma parameters.

The proposed NPA can be designed on a basis of the NPA ISEP (Ioffe institute) installed now on JET. A pellet light-gas gun can be used to accelerate Li pellets of $2 - 3$ mm in size up to 1 km/s velocities. That provides the required pellet penetration into the plasma core. Due to sticky problems with Li operation, a special technique of loading and keeping the pellets in a charger unit of LPI has to be developed.

Development of PCX diagnostics for absolute measurements of the confined minority protons requires improvement of the pellet ablation model used. Knowledge of the cloud dimensions and density distributions of different charge states of ions is of special interest. It is necessary to improve predictions of pellet penetrations in non-Maxwellian plasmas as well. An optical system for measurements of pellet cloud density profiles should be foreseen on W7-X.

1. Introduction

Understanding of fast particle behaviour in high-temperature magnetically confined stellarator plasmas becomes more and more important while plasma parameters increase to the reactor-like level. One of the goals of the stellarator W7-X is the demonstration of a good α-particle confinement in reactor extrapolation. However, the W7-X machine does not aim at DT operation. Therefore investigation of other fast ions in MeV range instead of α-particles, for instance fast hydrogen ions produced by Ion Cyclotron Resonance Heating (ICRH) can meet this goal in W7-X. This paper is devoted to assessing the diagnostics of fast H^+ ions based on charge exchange process in pellet ablation cloud. In Part 2, the general consideration of this problem is given. Different charge exchange schemes for diagnostics of protons are compared in Section 2.1, the physical basis of pellet charge exchange diagnostic is discussed in Section 2.2 and a set of PCX apparatus for W7-X is described in Section 2.3. Part 3 is devoted to Li pellet injection into W7-X plasmas. In Section 3.1, Li pellet ablation and penetration are simulated using the pellet ablation model that is described in Appendix. The pellet size and velocity required to penetrate the W7-X plasma are determined here. In Section 3.2, a pellet injection system is briefly considered. Section 3.3 considers a Li pellet ablation cloud as a target for charge exchange of fast protons. Part 4 is devoted to studies of H^+ RF-driven minority ion spectra in W7-X. In Section 4.1 the prototype of Neutral Particle Analyser (NPA) is proposed. Section 4.2 describes the model for ICR-heated minority spectra in W7-X. In Section 4.3, calculations of the count rates of neutralised protons for different scenarios of ICRF heating of H^+ minority in deuterium plasmas are presented. These calculations allowed us to formulate restrictions on a range of plasma densities of interest. Finally, in Part 5, conclusions are formulated and further possible steps for the development of PCX diagnostic for W7-X are discussed.

2. General consideration

2.1. Comparison of different charge exchange schemes

Fast ions with energy in sub MeV and MeV range can be produced in the W7-X stellarator by ICRF heating of H^+ minority in deuterium plasma. During the Neutral Beam heating there will be also deuterium beam ions with the energy ~ 100 keV. The specific features of fast ions can lead to the following main ion losses:

a) Orbit losses. Fast ions gyroradii are much larger than those of thermal ions. It leads to greater excursions of their orbits;

b) Ripple losses, ripple induced diffusion. Fast ions are much more sensitive to magnetic field ripple than thermal ions;

c) Losses caused by MHD instabilities existing in the plasma and also induced by the presence of fast ions (like Alfven eigenmodes).

The goal of fast ion studies is to understand the influence of the loss mechanisms listed above and other effects on the energy distribution function $f(E,r,t)$ of fast ions. Therefore, measurement of $f(E,r,t)$ over the plasma cross section and at various pitch angles (to get information about the velocity distribution function $f(v,r,t)$) is the main aim of fast ion diagnostics. For instance, it will be very interesting to measure the radial distributions of fast ions with different energies and pitch angles in quiescent plasmas and the re-distributions of the ions in the presence of various MHD events. These experimental results could be compared with the results of ion confinement modelling and could give the possibility to approve and develop or reject those models.

The promising diagnostics for the measurements of a fast ion distribution function is the neutral particle analysis. It is based on neutralisation of fast ions in the plasma and subsequent measurement of the energy distribution and the intensity of escaping atoms with a use of High Energy Neutral Particle Analysers (NPA).

Single charged hydrogen ions in MeV range can be neutralised by following ways.

Passive CX:

a) Charge exchange (CX) with residual H^0 or D^0 atoms in the plasma;

b) CX with [H]-like impurity ions (like C^{+5} and Be^{+3});

c) Recombination with plasma electrons.

Cross sections for proton charge exchange with D^0 [1] atoms and with C^{5+} ions [2] are presented in Fig.1. It is seen that the process a) takes place mainly in the energy range E<200 keV and process b) in E>200 keV. Recombination with plasma electrons usually is negligible in comparison with these two processes.

Active CX:

a) CX on hydrogen, deuterium or helium atomic beams – beam charge exchange (BCX);

b) Neutralisation in the pellet ablation cloud - pellet charge exchange (PCX).

The more attractive are the active CX measurements because they enable to get local ion distribution functions. For BCX option it is possible to use one of the W7-X

neutral heating beams (D^0, 100 keV, ~5 MW) or the diagnostic neutral beam with the parameters of the same scale.

In the case of *BCX* the energy spectrum of the detected atomic flux density per unit solid angle $d\Gamma_0/dE$ (atoms/(m^2·s·strd·eV)) correlates with the energy distribution of fast protons dn_{H^+}/dE as:

$$\frac{d\Gamma_0}{dE} = \frac{1}{4\pi} n_b \sigma_{cx}(v_{rel}) v_{rel} h \frac{dn_{H^+}}{dE} \qquad (1)$$

where n_b is the density of beam atoms, $\sigma_{cx}(v_{rel})$ is CX cross section versus relative ion-beam v_{rel} velocity and h is the beam dimension along the observation line. The absolute measurements are possible but due to a decrease of σ_{cx} with the energy (see fig. 1) they are possible only in the relatively low energy range (up to ~200 keV).

In the case of *PCX* the energy distribution of detected flux of atoms per unit solid angle is under certain conditions (see Section 2.2 below) given by:

$$\frac{d\Gamma_0}{dE} = \frac{1}{4\pi} v_{H^+} F_{0e}(E) \frac{dn_{H^+}}{dE} \qquad (2)$$

where v_{H+} and n_{H+} are the fast proton velocity and the density in the plasma, $F_{0e}(E)$ is the efficiency of neutralisation of fast ions in the pellet cloud. The computed $F_{0e}(E)$ for CX of protons on Li$^+$ target formed by Li pellet ablation cloud changes within the range of 10^{-2} – 10^{-5} (see Section 3.3). The details of PCX physical basis are presented below in Section 2.2.

For protons with the energy of 0.5 MeV, the ratio of BCX to PCX neutral flux density could be estimated using equations (1),(2)

$$\frac{d\Gamma_0/dE^{BCX}}{d\Gamma_0/dE^{PCX}} \cong \frac{n_b \cdot h \cdot \sigma_{CX}(E)}{F_{0e}(E)} \cong \frac{10^{10}(\text{cm}^{-3}) \cdot 10^{1 \div 2}(\text{cm}) \cdot 10^{-21}(\text{cm}^2)}{10^{-3}} \approx 10^{-(6 \div 7)}$$

We see that in the case of the PCX scheme, the neutral fluxes are much higher than those expected for the BCX scheme. Thus, the PCX diagnostics enables us to measure the fast ion distribution along the pellet track in one pellet shot. It provides a radially resolved energy spectra with the radial resolution ~ 1-3 cm. This allows detecting the ion redistribution caused by MHD activity right after or in the process of MHD event with good statistics, injecting the pellet in the proper moment of time. The PCX measurements are possible only in one particular moment of a discharge. The next pellet injection can be made after a period of two or three plasma confinement times.

2.2. Physical basis of PCX diagnostics

Good demonstration of PCX abilities has been presented in the studies of both DT alpha particles and RF-driven minorities on TFTR in 1995–98 [3]–[6], [13]. The PCX diagnostics was developed in co-operation between General Atomics, the A. F. Ioffe Physical Technical Institute, and the Princeton Plasma Physics Laboratory and operated routinely during DT experiments on TFTR [3]. Many PCX diagnostics results have been reported. They include measurements of RF-driven energetic helium-3 [4], hydrogen [5] and tritium [6] minority ion tails, the energy distribution of fast confined DT α particles and tritons [7], [8]. The influence of magnetic field ripple [9], sawtooth oscillations [10] and TAE modes [11] on the behaviour of the alpha energy spectra and radial density distributions has been studied.

The principal scheme of PCX diagnostic is shown in Fig. 2. Low-Z impurity pellets (Li, B or C) are injected along the midplane major radius. After entering the plasma, the pellet forms a toroidally elongated ablation cloud. A possible charge changing reaction for H^+ ions passing through a Li pellet cloud is:

$$H^+ + Li^+ = H^0 + Li^{2+}. \tag{3}$$

Depending on the cloud composition, other charge states of Li (Li^0, Li^{2+}) could also contribute to neutralisation of protons.

In a case when the line integrated cloud density for the particles traversing the cloud is sufficiently high, a fraction of particles emerging as neutrals approaches the equilibrium fraction F_{0e}, which is independent of the cloud linear density. A sample of $F_{0e}(E)$ for H^+ in a Li^+ target calculated in Ref. [12] is shown in Fig. 3 as a function of the particle energy E. Since the pellet cloud produces a fairly dense target for protons, an important question arises - whether the incident fast protons can suffer from significant angular scattering and/or from the energy losses in the cloud. This problem is discussed in Section 3.3 where scattering and the energy losses are shown to be insignificant for the range of proton energies and line integrated cloud densities of interest. This allows us to use equation (2) for calculations of the neutral flux density of the recharged particles per unit solid angle.

Neutrals escaping from the pellet ablation cloud can be mass and energy analysed using a Neutral Particle Analyser. The new NPA ISEP which can be used as a prototype for the W7-X PCX diagnostics has been recently developed in the Ioffe Institute. It is

described below in Section 4.1. Taking into account eq. (2) we have the following expression for the PCX signal – the number of counts of H^0 atoms by the NPA:

$$N(E) = n_{H+} \cdot f_{H+}(E) \cdot \Delta E \cdot v_{H+} \cdot S \cdot \frac{\omega}{4\pi} \cdot F_{0e}(E) \cdot K(E) \cdot \mu(E) \Delta t \text{ (particles). \quad (4)}$$

Here, E is the energy of the detected particles, v_{H+} is the velocity associated with energy E, n_{H+} and $f_{H+}(E)$ are the density and the distribution function of fast protons in the plasma, ΔE is the energy width of the NPA channel, S is the area of the portion of ablation cloud observed by the NPA, ω is a solid angle of NPA collimator, $F_{0e}(E)$ is the neutral equilibrium fraction, $K(E)$ is the calibrated NPA detection efficiency, Δt is the duration of the signal detection, $\mu(E)$ is the plasma transparency for H^0 atoms outcoming from the plasma:

$$\mu(E) = \int_L n_e(x) \cdot \sigma_{stop}(E) dx . \qquad (5)$$

Here, $n_e(x)$ is the plasma electron density, $\sigma_{stop}(E)$ is the H^0 stopping (re-ionisation) cross section which is a sum of cross-sections of electron ionisation, proton (deuteron) ionisation and ionisation by resonant CX, L is the way of H^+ atoms outside from the plasma. The values $\sigma_{stop}(E)$ are presented in Fig. 4. Equation (4) allows to obtain the energy spectra of protons $n_{H+} f_{H+}(E)$ from the detected number of counts $N(E)$ detected by the NPA. The expected NPA signals on W7-X are calculated in Section 4.3.

For illustration of the ability of PCX diagnostics to obtain the H^+ minority density profile we present here Fig. 5. It shows a radial profile of the 0.72 MeV H^+ ion density accelerated by fundamental H^+ ICRF heating. The profile has been measured by the PCX diagnostic in a TFTR deuterium plasma [13]. The measurements with the use of a look-down photodiode array were used to convert the Li pellet-induced PCX signal from the time domain to radial position in the plasma. In Fig. 6 also taken from Ref. [13] two spectra measured in discharges of similar parameters are compared: the active energy spectrum of ICRF-driven H^+ ions and the passive spectrum averaged over 100 ms during ICRF power pulse. It is seen that active and passive spectra have the same Maxwellian shapes and very similar effective tail temperatures.

2.3. PCX apparatus on W7-X

PCX experimental set-up proposed for W7-X is presented in Fig. 7 a, b) (poloidal and top-of view of the set-up correspondingly). The pellet injector (PI) axis is located

horizontally about 10cm above a midplane major radius of W7-X in the port AEE-41. The NPA viewing line is located in the same horizontal plane at the angle of $\sim 2^0$ to the PI axis. PI (50×80×80 cm) together with the NPA (50×80×80 cm) are placed on one platform that provides the scan of the plasma in toroidal direction within the angle range of about 0-6^0. Probably, it allows the detection of particles having different pitch angles. The distance of 5-6 meters between the plasma axis and the platform could provide a significant reduction of noise level in NPA (see below). A pellet velocity and a pellet radial position are detected with the collimated photodiode array (CFA, 10×80×10 cm) and the CCD camera (CAM1, 15×30×30 cm), which is located in the port AEF-41. This CFA view lines (7 – 10 chords) intersect the pellet trajectory with 3 – 4 cm intervals in the plasma midplane. Total emission of the pellet cloud is measured by the wide-view detector (WVD, 10×10×10 cm) and by two CCD cameras (CAM1, CAM2) equipped by interference light filters. The WVD detector and CAM2 camera are placed on the platform nearby PI in the main entrance port AEE-41. By combining the CFA and WVD pellet time-in-flight measurements with the time dependence of the observed PCX neutral signal, the radially resolved particle energy spectra and the pellet ablation rate profiles can be derived with a radial resolution of 1–3 cm. Optical system for measurements of pellet cloud densities could be foreseen as well.

3. Li pellet injection into W7-X plasmas

3.1. Li pellet ablation and penetration

A possibility of PCX diagnostics to obtain the H^+ distribution function in the core plasma region depends on the pellet penetration depth. Therefore it is important to determine the pellet velocity that will provide pellet penetration into the plasma centre. Furthermore, the derivation of the energy spectra of protons from the count rate of neutralised protons at the NPA requires knowledge of the ablation cloud dimensions (see Section 3.3). For these purposes the simulations of Li pellet ablation in W7-X were performed.

Because a high pellet ablation rate values are expected we used an approach proposed in Ref. [31] where an impurity pellet ablation is considered on a base of hydrogen pellet ablation model [14] with an almost complete shielding of pellet surface. In the model developed, kinetic effects of heat flux penetration through the neutral cloud are considered

two-dimensionally. The model takes into account the effect of "cloud charging" (See Ref. [14] and references in it), i.e. the potential drop at the cloud boundary, which is determined from the balance between the electron and ion currents falling onto the cloud and the current of cold electrons leaving the cloud. The model enables us to take into account fast ions, which appear in the presence of Neutral Beam Heating, and suprathermal electrons. To simplify calculations we have made simulations considering only Maxwellian distribution of electrons and ions. Such a simplified model as well as its verification by Heliotron-E and W7-AS experimental results are described in the Appendix. This model doesn't take into account a possible increase of ablation due to influence of non-maxwellian electrons (suprathermals), hot minority ions created by ICRH and/or bulk plasma ions heated by NBI. A plasma scenario when the electron temperature profile is determined mainly by ECR heating power and the ICR heating determines H^+ minority population was considered for calculations of Li pellet ablation and penetration into W7-X plasmas. This means that the results of our simulations give low-level estimations of the ablation rate and pellet velocities required for its penetration to the plasma core.

Plasma density and electron temperature profiles

$$n_e(r) = n_e(0)/(1 + r/0.73)^6 \qquad (6)$$

$$T_e(r) = T_e(0) \cdot (1-(r/a)^2) \qquad (7)$$

as well as ion temperature profile were taken from Ref. [15]. A simulated dependence of the central electron temperature on the ECR heating power for different plasma densities from Ref. [15] is shown in Fig. 8.

In our simulations the pellet size was chosen such that the total amount of electrons in the pellet is equal to the electron content of the ambient plasma prior to pellet injection. This condition provides an acceptable plasma disturbance by pellet injection that is confirmed by Li pellet experiments on Heliotron-E [16]. To be confident in pellet penetration to the central zone we imposed that a pellet should keep 20% of its atoms when it arrives at the plasma axis. For calculation of pellet ablation in plasma core the adjusting parameter value $r_i \sim 0.2$ cm (see Appendix) was used.

The dependence of the pellet velocity required for core penetration on the ECRH heating power is shown in Fig. 9 for central plasma density 10^{13} cm^{-3} (solid line), $5 \cdot 10^{13}$ cm^{-3} (dashed line) and 10^{14} cm^{-3} (dotted line). One can see that the range of the required pellet velocities is 200 – 1000 m/s. A sample of the ablation profile for a spherical Li pellet $\varnothing 2.1$mm in size and 670 m/s velocity is shown in Fig. 10 for plasma density $\sim 5 \cdot 10^{13}$ cm^{-3}

and electron temperature ~ 5.6 keV that corresponds to the 8 MW ECRH power. These parameters are shown in Section 4.3 to be the best conditions for detecting H^0 energy spectrum.

3.2. Pellet injection system

The dependence of Li pellet velocities that could be obtained in one-stage light gas–gan with barrel length $L_b = 120$ mm and diameter $d_b = 2.5$ mm on the propellant (He) gas pressure is shown in Fig. 11. It is seen that a light-gas gun can provide the required range of pellet velocities for pellet of about 2-3 mm sizes.

The main technical problem of the Li pellet injection system might be a sticky problem due to a big chemical activity of Li [17], [18]. Being pressed on steel plate the lithium feels in the harshness of the metal surface and easily sticks to it. This requires development of a special technique for loading the pellets into the charger unit of the injector that should provide reliable acceleration of Li pellets under remote control during some days after loading.

3.3. Li pellet ablation cloud as a target for charge exchange of protons

To use equation (4) for the calculation of the fast proton energy spectrum by means of the number of NPA counts, the following conditions should be fulfilled:

a) The fraction of particles emerging from the cloud as neutrals attains its equilibrium fraction.

b) Energy losses and angular deviation of protons in the cloud are insignificant.

The conditions should be fulfilled for the range of both fast proton energies and line integral cloud densities expected for W7-X experiments.

To verify these conditions we need the information about the density distributions of Li^+, Li^{2+} and Li^{3+} ions in the pellet cloud. This information would enable us to estimate the expected range of line integral cloud densities for W7-X and also the area of the observed part of the cloud in the equation (4). Unfortunately, there is a lack of information about the required density distributions. Therefore, we made evaluations of the line-integrated cloud densities in a way similar to those that has been done in Ref. [12].

The density of the Li pellet cloud of about $n_{cl} \sim (1-2) \cdot 10^{17}$ cm^{-3} was evaluated in Ref. [19] using measurements of the line broadening of Li^+ ions (585.5 nm). This value was averaged over the whole ablation time of the Li pellet injected into an Ohmic heated TFTR shot. On the other hand, the time resolved Stark broadening measurements during the

9

hydrogen pellet ablation in TFTR and PLT (see Ref. [20]) show that the pellet cloud density increases almost proportionally to the pellet ablation rate. Therefore, the estimation of Li cloud density $(2 \div 3) \cdot 10^{17}$ cm^{-3} is most likely the upper value, i.e. the value in the maximum of ablation. Then, the estimation of the line integrated cloud density is a product of 10^{16} - $3 \cdot 10^{17}$ cm^{-3} and the cloud dimension along the NPA observation line. Usually, the observation line is almost normal to the magnetic field direction. Therefore below we consider the cloud size in the direction transverse to the local magnetic field direction.

3.3.1. Evaluations of Li$^+$ cloud transverse size and line-integrated densities

It is known that an ablation cloud is stretched along the magnetic field lines and has a "cigar" shape with the length much greater than the radius. Example of an image of Li$^+$ cloud in TFTR (#52197, $n_e(0) \approx 6.8 \cdot 10^{13}$ cm^{-3}, $T_e(0) \approx 2.3$ keV) from Ref. [12] is shown in Fig. 12. In Ref. [12] the Li$^+$ cloud radius r_{cl} was estimated as several centimetres. For the following reasons it seems to us that this is an overestimation and r_{cl} is of the order of millimetres.

1) The millimetre range of r_{cl} was observed in T-10 carbon pellet experiments. In Fig. 13a, the cloud intensity in the poloidal (dashed curve) and toroidal (solid curve) direction derived from a snap-shot (40 μs exposure time, a total visible range of light) are shown. The characteristic decay length in the poloidal direction that can be interpreted as r_{cl} is shown versus minor plasma radius in Fig. 13b together with the carbon pellet ablation rate profile and radial profile of the ionisation radius of carbon cloud calculated using eq. (8) (see below). It is seen that both transverse sizes have a millimetre range of magnitude.

2) We also estimated r_{cl} for TFTR #52197 as the ionisation length of Li^0 atoms:

$$r_{cl} = c_s \tau_{ion} \qquad (8)$$

where $c_s = \sqrt{\dfrac{5}{3} \dfrac{k_{Bol} T_s}{m_a}}$ is the velocity of evaporated atoms, $T_s = 1700$ K is Li pellet surface temperature, m_a is the mass of Li^0 atom, $\tau_{ion} = \dfrac{1}{n_e R(T_e)}$, n_e(cm^{-3}) being the plasma electron density, $R_1(T_e) = \sqrt{\dfrac{I_1}{T_e}} \left(4.5456 \cdot 10^{-8} \, ln\left(\dfrac{T_e}{I_1}\right) + \sum_{n=0}^{2} \beta 1_n \left(\dfrac{I_1}{T_e}\right)^n \right)$ (cm^3/s) is the ionisation rate to the first state, T_e(eV) is the plasma electron temperature, $I_1 = 5.39$ eV, $\beta 1_0 = 2.78 \cdot 10^{-7}$, $\beta 1_1 = -1.583 \cdot 10^{-6}$, $\beta 1_2 = 5.465 \cdot 10^{-6}$ [21]. The estimated r_{cl} versus effective minor radius of TFTR is shown in Fig. 14 by the dashed line.

10

3) We made the estimation of r_{cl} for TFTR #52197 from the energy balance. Lets consider the balance of the electron heat flux flowing onto the cloud from the bulk plasma and the energy required to evaporate, ionise and heat the evaporated material:

$$2\pi r_{cl}^2 Q_e = \dot{N}\left(\varepsilon_{ion} + \varepsilon_{subl} + \varepsilon_{heat}\right) \qquad (9)$$

where $Q_e = n_e\sqrt{\dfrac{2T_e^3}{\pi m_e}}$ is the plasma electron heat flux density, $\varepsilon_{ion} = 5.39$ eV/at is the first ionisation energy for Li, $\varepsilon_{subl} = 2.089$ eV/at is the sublimation energy for Li, $\varepsilon_{heat} = 1$ eV/at is the energy required to heat the neutral ablatant up to 1 eV, $\dot{N}$ is the pellet ablation rate. The result of this evaluation of r_{cl} for TFTR is shown in Fig. 14 by the solid line.

It is seen from Fig. 14 that for TFTR #52197 the estimation of the cloud radius from both the energy balance and ionisation radius give $r_{cl} \approx 1$ mm which is about of one order of magnitude less than the estimation made in Ref. [12].

4) In Ref. [12] the PCX-measured alpha-particle energy distribution in TFTR #86291 (small black boxes in Fig. 15 here and in Fig. 15 of Ref. [12]) had a smaller magnitude than the FPPT-code predictions (solid line in Fig. 15 here and in Fig. 15 Ref. [12]). We suppose that one of the reasons of such disagreement could be an overestimated value of the effective cloud area, from which neutrals are detected by the NPA (S in eq. (4)). To evaluate S we should consider the geometry of the experiment. Only a part of the cigar-shaped cloud which intersects with the solid view angle of the NPA $d\Omega$ can be observed. In the experiments at TFTR the radius of the visible part was r_{NPA} ~2.5 cm at ~6 m from the NPA. In Ref. [12] the Li pellet cloud radius was estimated as $r_{cl} > 2.5$ cm and therefore the area of the part of the cloud from which neutrals are collected is $S = \pi$ $(r_{\text{NPA}})^2 \approx 20$ cm^2. Fig. 16 a) illustrates this situation. Our estimations give $r_{cl} \approx 1$ mm $\ll$ r_{NPA} and the effective cloud area from which neutrals are detected depends on the cloud radius as $S = 4\, r_{cl}\, r_{\text{NPA}} \approx 1$ cm^2 - see Fig. 16 b). Using $S \approx 1$ cm^2 instead of $S \approx 20$ cm^2 in eq. (4) to deduce the energy spectra for TFTR #86291 from the measured number of the NPA counts, one can obtain the curve shown by the large boxes in Fig. 15 here. The corrected alpha energy distribution function is evidently closer to the theoretical (solid) curve. So the overestimation of the values of r_{cl} and S is possibly one of the reasons of the disagreement of the PCX measured and expected alpha energy distribution in Ref. [12]. Another possible reason of this disagreement is the lack of information about the cloud charge state

composition. An influence of this effect on our calculations of the NPA counts will be discussed below.

Thus, we imply that $r_{cl} \sim 1$ mm holds also for W7-X. We estimated r_{cl} from the energy balance as well as the ionisation radius of the cloud. Results are shown in Fig. 17 by the solid and dashed line correspondingly. The ablation rate $\dot{N}$ in eq. (9) is the pellet ablation rate which was found in Section 3.1 as a function of effective plasma minor radius. From Fig. 17 it follows that $r_{cl} \approx 1$-2 mm for W7-X. using these r_{cl} values and 10^{16} - $3 \cdot 10^{17}$ cm^{-3} values for Li$^+$ cloud densities, the line integrated density range expected for W7-X is 10^{15} - $5 \cdot 10^{16}$ cm^{-2}.

3.3.2. Neutral fraction of particles emerging from Li cloud

The flux of protons incident on the Li target with density n_{Li} diminishes with the growth of the target thickness x as protons are neutralised through CX. This process is described by the set of equations (see Ref. [12])

$$\frac{dn_0}{dx} = \left(n_1 \cdot \sigma_{10} - n_0 \cdot \sigma_{01} \right) \cdot n_{Li}, \tag{10}$$

$$\frac{dn_1}{dx} = \left(n_0 \cdot \sigma_{01} - n_1 \cdot \sigma_{10} \right) \cdot n_{Li} \tag{11}$$

$$n_1(x) + n_0(x) = n_0(0) \tag{12}$$

where n_0 and n_1 are the densities of H^0 and H$^+$ respectively, and σ_1, σ_{01} are correspondingly the cross sections of proton neutralisation and H^0 ionisation in the cloud. If the cloud is composed of k_1 % Li$^+$, k_2 % Li^{2+} and k_3 % Li^{3+} then

$$\sigma_{10} = 0.01 \cdot \left(k_1 \sigma_{10}^{(1)} + k_2 \sigma_{10}^{(2)} \right), \tag{13}$$

where $\sigma_{10}^{(1)}$, $\sigma_{10}^{(2)}$ are correspondingly the cross-sections of proton neutralisation in Li$^+$ and Li^{2+} target. For H^0 ionisation cross-section we have

$$\sigma_{01} = 0.01 \cdot \left(k_1 \sigma_{01}^{(1)} + k_2 \sigma_{01}^{(2)} + k_3 \sigma_{01}^{(3)} \right). \tag{14}$$

Electron recombination is neglected as was done in Ref. [12]. Electron impact ionisation may be included into σ_{01}. Fig. 18 a,b shows $\sigma_{10}^{(1)}$ and $\sigma_{01}^{(1)}$ and Fig. 19a,b shows $\sigma_{10}^{(2)}$ and $\sigma_{01}^{(2)}$ from Ref. [22].

It follows from eqs. (10) – (12) that the fraction of particles emerging as neutrals from the cloud $F_0(E, S_n)$ depends on their energy E and on line integrated cloud density

$$S_n = \int_L n_{Li^+} dx \text{ as}$$

$$\frac{n_0}{n_0 + n_1} = F_0(S_n, E) = \frac{1 - exp\left(-\left(\sigma_{01}(E) + \sigma_{10}(E)\right) \cdot S_n\right)}{1 + \sigma_{01}(E)/\sigma_{10}(E)}. \qquad (15)$$

For large S_n values, F_0 attains its equilibrium value

$$F_{0e}(E) = \frac{1}{1 + \sigma_{01}(E)/\sigma_{10}(E)} \qquad (16)$$

which can be also obtained by setting the left-hand sides of eqs. (10) and (11) to zero.

It follows from eqs. (13), (14), (16) that in order to calculate $F_{0e}(E)$ we need the information about cloud charge state composition. Such information is not yet available either theoretically or experimentally. Therefore an assumption about cloud composition should be made. In Fig. 20 the equilibrium neutral fraction is shown for different cloud charge state compositions for the energy range of H^0 and H^+ 100 keV÷1 MeV. Thick solid line corresponds to 100% of Li^+, dashed line – 50% Li^+ and 50% Li^{2+}, dotted line - 30% Li^+ and 70% Li^{2+}. For comparison, the equilibrium fraction of H^0 in 100% of Li^+ cloud calculated in Ref. [12] is shown by the thin solid line. It is seen from Fig. 20 that the relative energy dependence of F_{0e} is the same for different cloud charge state composition. Therefore, the proton energy spectrum being deduced from the NPA signal is insensitive to the cloud composition. But the absolute values of $F_{0e}(E)$ calculated under assumption that the cloud is composed purely of Li^+ might be overestimated.

Fig. 21a,b shows the dependence of the fraction of neutralised protons in Li cloud on S_n in the range 10^{15} cm^{-2} ÷ 10^{19} cm^{-2}. Fig. 21a is $F_0(S_n)$ in 100% Li^+ cloud for the energy of protons $E = 100$ keV (solid line), $E = 500$ keV (dashed line), $E = 1$ MeV (dotted line). Fig. 21b is $F_0(S_n)$ for proton energy 500 keV in 100% Li^+, 50% Li^+ 50% Li^{2+} and 100% Li^{2+} cloud. Calculations show that for higher energies and greater Li^+ content in the cloud the neutral fraction reaches its equilibrium value at higher S_n. It follows from Fig. 21 that in the energy range of interest (100 keV ÷ 1 MeV) the neutral fraction of protons in Li cloud attains its equilibrium value only for highest values of the expected line–integrated densities ($5 \cdot 10^{16}$ cm^{-2}). Because of the lack of information about cloud charge state composition the absolute measurements of fast ion energy spectra are difficult. An optical system for measurements of pellet cloud densities should be foreseen on W7-X.

3.3.3. Energy losses and angular scattering of protons in a Li cloud

If the cloud is too dense, the incident fast protons can suffer significant angular scattering and energy losses in the cloud. We made the corresponding evaluations for fast

13

hydrogen ions in the range of H^+ energies (100 keV – 1 MeV) and line integrated cloud densities (10^{16} – $5 \cdot 10^{16}$ cm^{-2}) expected for W7-X plasmas.

Cloud electrons (bound and unbound) are responsible for most of the energy loss of fast protons in the cloud. The combined energy loss may be written as

$$\frac{dE}{dx} = L(E) \cdot n_{Li} \tag{17}$$

where n_{Li} is the cloud density,

$$L(E) = Z_{Li} \cdot 0.96 \cdot 10^{-16} \cdot E(eV)^{0.4} \left[eV \cdot cm^2 \right] \tag{18}$$

is the loss function for protons in neutral hydrogen [23] multiplied by number of electrons in the impurity atom ($Z_{Li} = 3$ for lithium). For the relative energy loss of a proton with initial energy E_0 in a Li cloud with line integrated density we used the following expression:

$$\frac{\Delta E}{E_0} = 1 - \frac{\left(E_0^{0.6} - 0.6 \cdot Z_{Li} \cdot 0.96 \cdot 10^{-16} \cdot S_n \right)^{\frac{1}{0.6}}}{E_0} \tag{19}$$

which was obtained by integrating eq. (17) with loss function (18).

Fig. 22 shows the relative energy loss (%) of a proton in Li cloud versus cloud line integrated density (cm^{-2}) for H^+ energy 100 keV (solid line), 500 keV (dashed line) and 1 MeV (dotted line). It follows from   Fig. 22 that energy losses of protons are much smaller compared to the expected energy resolution $\Delta E = (0.05 - 0.1) E$ of the NPA. Therefore the energy of neutrals escaping from the cloud fairly well corresponds to the energy of fast protons entering the cloud. It is clear that unknown composition of the pellet cloud could not bring a significant increase of the energy losses.

Mean square angular deviation of a proton due to multiple small angle collisions of ions of charge Z was found from the following equation [24]

$$\langle \Theta^2 \rangle \approx 4\pi S_n \left(\frac{Z Z_p e^2}{E_p} \right)^2 ln \left(\frac{\theta_{max}}{\theta_{min}} \right) \tag{20}$$

which is derived from the classical Rutherford scattering formula. Here $Z = 1$ for Li^+, $Z = 2$ for Li^{2+}, $Z_p = 1$ for a proton, E_p is the energy of a proton,

$$\theta_{min} = \frac{Z^{1/3} c}{192 v^2}, \qquad \theta_{max} = \frac{274 c}{A^{1/3} v^2}$$

where A is the atomic mass number of an impurity ion ($A_{Li} = 6.9$) and v is the relative ion – proton velocity. Fig. 23 shows the mean square scattering angle (grad) of a proton in 100%

Li$^+$ cloud versus its energy (MeV) for cloud line integrated density equal to 10^{15} cm^{-2} (solid line), 10^{16} cm^{-2} (dashed line) and 10^{17} cm^{-2} (dotted line). This mean square scattering angle will be two times greater for 100% Li^{2+} cloud, and 1.6 times greater for 50% Li$^+$, 50% Li^{2+} cloud. Therefore, it could be seen that an angular scattering of protons in Li cloud is small. Hence, the information about H$^+$ pitch-angle is saved during CX in the cloud.

4. Studies of H$^+$ RF-driven minority ion spectra in W7-X

4.1. Prototype of the Neutral Particle Analyser

Fig. 24 presents a schematic drawing of the NPA. The operation of this instrument is based on ionisation of atoms by stripping in a thin carbon foil (~300 A) and analysis of the secondary ions in co-linear magnetic and electric fields. The analysing 180^0 magnet has a profiled magnetic gap designed with the use of special particle tracking program. The analysing condenser plates are not parallel in accordance with the recommendations of the same program. The special shape of magnetic gap and analysing condenser plates provides good focusing the deuterium and hydrogen ions into detectors. The NPA has two parallel detector arrays for protons and deuterons. Each array consists of 25 small scintillation detectors based on photomultiplier tube (PMT) equipped with thin CsI(Tl) scintillators of micron thickness. Full energy range of the NPA is 10 – 1000 keV for protons. The dynamic energy range is $E_{max}/E_{min} = 5$. The energy resolution of the NPA channels $\Delta E/E \sim 5 - 10$ %. Mass rejection between H and D detectors is better than 10^{-2}. The NPA has two parallel detector arrays for protons and deuterons.

Having the detection efficiency for ions equal to almost 100% those detectors have very low gamma and neutron detection efficiency equal to $\sim 10^{-5} - 10^{-6}$ per neutron. The use of such neutron-gamma insensitive detectors is important in W7-X conditions. Note that the W7-X deuterium plasma with deuterium NBI heating will produce up to $6 \cdot 10^{15}$ neutrons/s [27]. On the basis of the experiments at TFTR and JET we can conclude that the neutron flux of $6 \cdot 10^{15}$ neutrons/s leads to $\sim 6 \cdot 10^7$ n·s^{-1}cm^{-2} at the location of the NPA detectors (5 – 6 m from the plasma axis) in the absence of any shielding. The neutron sensitivity of microchannel plates, channeltrons and other electron multipliers is equal to $\sim 10^{-3}$. This means that the background count rate of the conventional microchannel plates, channeltrons and other open electron multipliers would be $\sim 6 \cdot 10^4$ s^{-1} without shielding.

15

However, the detectors of the ISEP will detect background count rate $10^2 - 10^3$ less. This means that ISEP will not require neutron-gamma shielding on W7-X.

The sensitive area of the detectors are located at the detector plane (see Fig. 24). The expected values of the detection efficiency for hydrogen atoms $K(E)$ versus the energy of atoms for the range of $50 - 1000$ keV is presented in Fig. 25. $K(E)$ values have to be obtained as a result of NPA calibration with the use of hydrogen atomic beam.

4.2. The model of ICR-heated minority spectra in W7-X

As it was mentioned above, the character of suprathermal ion losses in the toroidally varying stellarator field of W7-X can be studied with the use of ions driven by ICRH. In the stage I of the W7-X experiments, it is planned to use two ICRH generators of 2 MW power each. For a second stage, a 12 MW system (six generators), 30 to 115 MHz of ICRH allowing minority heating (H in D) in the machine is envisaged [28]. For estimation of PCX H^+ signal we use the following expressions for H^+ tail energy distribution function $f(E)$ in accordance with the Stix predictions [29]:

$$f_{H^+}(E)\, dE \sim (E)^{1/2} \cdot \exp\left(-\frac{E}{T_{Stix}}\right) dE, \qquad (21)$$

where T_{Stix} is H^+ tail temperature expressed as

$$T_{Stix} = \frac{P_{RF}\tau_{sl}}{n_{H^+}V}. \qquad (22)$$

Here P_{RF} — RF power absorbed by H^+ minority, V — volume of the plasma , n_{H^+} — the density of H^+ minority, τ_{sl} — classical slowing down time. For calculation of τ_{sl} we used

$$\tau_{sl}(s) = 4 \cdot 10^7 \frac{T_e^{3/2}(eV)}{n_e\left(cm^{-3}\right)}. \qquad (23)$$

Here T_e is electron temperature, n_e — electron density. For the estimations we assume that $n_{H^+} = 0.05\ n_e(0)$, $V = 2\pi R \cdot \pi a^2 = 3.2 \cdot 10^7$ cm^3 (values $R = 550$ cm, $a = 55$ cm were taken from [28]), n_e and T_e are given by eqs. (6) and (7).

4.3. Calculation of NPA signals

Using the ablation cloud parameters (Section 3.3), the NPA parameters and the modelled energy distribution function of fast protons (Section 4.2) we can estimate the magnitude of the NPA signal from eq. (4). The following NPA parameters were used in the calculations of the NPA signal: $K(E)$ — see Fig. 25, $\Delta(E) = 0.1\ E$, $\omega = 4 \cdot 10^{-6}$ strd. The

16

integration time of NPA channels is $\Delta t = \dfrac{a}{10} \cdot \dfrac{1}{v_{pellet}} \sim \dfrac{3cm}{10^5 cm/s} = 3 \cdot 10^{-5}$ s. This means

that the energy distribution function will be measured with ~ 3 cm spatial resolution.

The area of the portion of ablation cloud observed by the NPA limited only by NPA collimator was equal to $S \approx 2$ cm^2 in accordance with the estimation of ablation cloud thickness The plasma transparencies for H^0 atoms $\mu(E)$ outgoing from the plasma centre of W7-X for $n_e(0) = (10^{13} - 10^{14})$ cm^{-3} are obtained by eq. (5) and presented in Fig. 26. For the integration we used radial plasma density profiles (6). It can be seen that the $\mu(E)$ values in W7-X for energy range of atoms > 50 keV are not far from 1. They have to be taken into account only for the plasma densities > $(8-9) \cdot 10^{13}$ cm^{-3}. W7-X regimes for which we estimated the PCX signal are presented in Table 1. Because of the absence of the information about Li cloud charge state composition we assumed a 100% Li$^+$ cloud. As was shown in section 3.3.2 above, such simplification doesn't affect the energy dependence of the proton energy spectra, but the absolute values of the NPA signals may be overestimated.

Fig. 27 presents PCX counts N(E) of the NPA calculated during time corresponding to a pellet flight of 3 cm distance in the plasma. The ICRF power is $P_{RF} = 3$ MW typical for stage I of the experiments and for different plasma densities in the range of $10^{13} - 9 \cdot 10^{13}$ cm^{-3}. It can be seen from Fig. 27 that PCX H^0 count rate is rather high. It is seen also that the best conditions for detecting H^0 energy spectrum correspond to medium plasma density $(3 - 5) \cdot 10^{13}$ cm^{-3}. Fig. 28 presents the same data for higher RF power $P_{RF} = 6$ MW. Here we have the same character of the N(E) dependence on the density but more high effective temperature of the N(E) spectra. The N(E) values for fixed plasma density $4 \cdot 10^{13}$ cm^{-3} and changing RF power is shown in Fig. 29. It can be seen from these plots that at the optimal density $(4 \cdot 10^{13}$ cm$^{-3})$ PCX count rate increases with the increase of RF power.

5. Conclusions and further steps

PCX diagnostics with the use of Li pellet can provide very well detectable H^0 signal in the range of 10 − 1000 keV generated by RF driven H$^+$ minority ions in W7-X. PCX diagnostics will be able to measure H$^+$ energy spectra and density profiles in wide range of W7-X plasma parameters.

The proposed NPA ISEP can detect also beam hydrogen and deuterium particles with E > 50 keV in the case of neutral beam heating in W7-X. It will give the possibility to study the energy spectra and radial profiles of those particles with the use of PCX diagnostics and also with the use of conventional passive and active CX diagnostics.

A pellet injection system should accelerate Li pellets of 2 – 3 mm in size up to 1 km/s velocities. It will enable pellets to penetrate to the plasma centre in W7-X without lethal plasma disturbance when a total amount of injected electrons does not exceed the total plasma content of electrons prior to pellet injection. A pellet light-gas gun can provide the desired range of velocities. Due to sticky problems with Li operation, a special technique of loading and keeping the pellets in the charger unit of the injector has to be developed. R&D of such a system and its combination with the pellet accelerator could be considered for the further activity.

Development of PCX diagnostic for absolute measurements of the confined minority protons requires improvement of the pellet ablation model. It is necessary to improve predictions of pellet penetrations in non-Maxwellian plasmas as well. Knowledge of the cloud dimensions and density distributions of different charge states of ions is of special interest for these absolute measurements. An optical system for measurements of pellet cloud density profiles should be foreseen on W7-X.

Appendix

Impurity pellet ablation model

V.Yu.Sergeev, B.V. Kuteev, O.A. Bakhareva, A. Yu. Kostrukov, V.G. Skokov

State Technical University, St.Petersburg, Russia

General Scheme

Fig. 30 gives a general description of pellet-plasma interaction. A spherical pellet is evaporated by heat fluxes of the electrons Γ_e and the thermal ions Γ_i. Moving only along the magnetic field lines $\vec{B}$, the electrons produce maximal ablation at the pellet poles ($\alpha = 0, \pi$). The ion flux from all the angles is assumed to be uniform. The neutrals leaving the pellet surface expand spherically and form a dense cloud, which reduces initial heat fluxes.

Being ionised at some distance from the pellet surface the neutrals produce a secondary plasma cloud expanding along the magnetic field lines. The conductivity of the cloud is high enough (both along and transverse the magnetic field) so that it can be considered equipotential. A substantial potential drop $\Delta\varphi$ takes place only near the boundary between the secondary plasma and the hot bulk plasma.

Cloud Potential

The magnitude of this drop $\Delta\varphi$ is determined by the balance of the incoming currents I_e, I_i and the outgoing current of the cold electrons I_{ec} as was proposed in Ref. [34]:

$$I_e = I_i + I_{ce}. \tag{a1}$$

These currents can be brought out as follows. Only the plasma electrons with velocities greater than v_{crit} pass through the potential barrier $\Delta\varphi$ at the cloud boundary.

$$v_{crit} = \sqrt{\frac{2e}{m_e}\Delta\varphi}, \tag{a2}$$

where e and m_e are electron charge and mass. This means that the electron current can be written in the form:

$$I_e = e2\pi r_p^2 \int_{v_{crit}}^{\infty} f_M v_z dv_z, \tag{a3}$$

where

19

$$f_M = \frac{n_e}{\sqrt{\frac{2\pi T_e}{m_e}}} exp\left(-\frac{m_e v_z^2}{2T_e}\right), \tag{a4}$$

n_e and T_e are electron density and temperature in the bulk plasma, r_p is the pellet radius.

The density of the cold cloud electrons passed into the bulk plasma is determined by the quasi-neutrality condition:

$$n_{e_{cold}} = \int_{-\infty}^{\infty} f_M dv_z - \int_0^{\infty} f_M dv_z - \int_0^{v_{crit}} f_M dv_z = \int_{v_{crit}}^{\infty} f_M dv_z. \tag{a5}$$

Here the first term is the ion concentration in the bulk plasma, the second one is the density of the electrons moving towards the cloud and the third one is the density of the electrons reflected by the potential barrier. The cold electron velocity after passing the potential drop is of the order of v_{crit}, so that their current is:

$$I_{e_{cold}} = e2\pi r_p^2 \sqrt{\frac{2e}{m_e}\Delta\varphi} \int_{v_{crit}}^{\infty} f_M dv_z. \tag{a6}$$

For the ion current I_i we use the following expression that is derived from [30]:

$$I_i = 0.3 Z_{pl} e n_e r_p^2 \sqrt{\frac{8\pi T_i}{m_i}} \left(1 + 0.75\Delta\phi^{0.68}\right) \left(1 + 0.564\left(\frac{T_i}{T_e}\right)^{0.797}\right)\left(3.052 - 0.32\, ln\left(\frac{r_p}{D}\right)\right), \tag{a7}$$

where m_i and Z_{pl} are the mass and charge number of a bulk plasma ion, T_i and D – ion temperature and Debye radius in the bulk plasma,

$$D = \sqrt{\frac{T_i}{4\pi Z_{pl} e^2 n_e}}. \tag{a8}$$

This is an improved expression compared to [14] where the Bohm expression was used for the saturated ion current.

The boundary between the hot initial plasmas and the dense secondary plasmas is considered one-dimensionally. In this case the substitution of (a3), (a6) and (a7) into the balance equation of currents (a1) yields the following expression for cloud potential:

$$exp(-x) - \sqrt{\pi x}\left(1 - erf\left(\sqrt{x}\right)\right) - $$

$$-0.6\sqrt{\frac{m_e T_i}{m_i T_e}}\left(1 + 0.75\Delta\phi^{0.68}\right)\left(1 + 0.564\left(\frac{T_i}{T_e}\right)^{0.797}\right)\left(3.052 - 0.32\, ln\left(\frac{r_p}{D}\right)\right) = 0. \tag{a9}$$

Here, $x = e\Delta\varphi/T_e$. With the pellet charging effect taken into account, the values of the heat fluxes on the neutral cloud boundary q_e and q_i corresponding to the electrons and ions subsequently can be written out as follows:

$$q_e = \frac{1}{4}\sqrt{\frac{8T_e}{\pi m_e}} 2T_e n_e \exp\left(\frac{-e\Delta\varphi}{T_e}\right) 2\pi r_p^2 , \qquad (a10)$$

$$q_i = 0.6 n_e r_p^2 \sqrt{\frac{8\pi T_i^3}{m_i}} \cdot \left(1 + 0.75\Delta\phi^{0.68}\right) \cdot \left(1 + 0.564\left(\frac{T_i}{T_e}\right)^{0.797}\right) \times$$

$$\times \left(3.052 - 0.32\ln\left(\frac{r_p}{D}\right)\right) \cdot \left(1 + \frac{e\Delta\varphi}{2T_i}\right) . \qquad (a11)$$

Heat Flux Penetration

The thermal fluxes falling onto the pellet surface are estimated at each point on the pellet surface separately (i.e. for the different α values , see Fig. 30).

Lets consider the case with no cloud charging. The density of the thermal flux penetrating through the cloud can be written as follows:

$$Q(S_n, \alpha) = Q_e\left(\frac{S_n}{\cos\alpha}\right)\cos\alpha + Q_i(S_n), \qquad (a12)$$

where

$$Q_{e,i}(S_n) = \frac{4\pi}{m_{e,i}^{1/2}(2\pi T_{e,i})^{1/2}} \int_0^1 \zeta d\zeta \int_0^\infty E^2 f_{e,i}(S_n, E, \zeta)\, dE . \qquad (a13)$$

Here e corresponds to electrons, i – to ions, $f_{e,i}(S_n,E,\zeta)$ and $f_{hi}(S_n,E,\zeta)$ are the distribution functions for the particles after penetrating through the optical length S_n, E is the particle's energy, m_e is the electron mass, m_i is the bulk plasma ion mass. S_n is considered as the optical length of the cloud in the direction perpendicular to the pellet surface.

$$S_n = \int_{r_p}^\infty n_a(r)\,dr , \qquad (a14)$$

where n_a is the atomic density of the cloud. The plasma shielding effect is neglected in our analysis, so that the secondary plasma parameters are not included in the expression for S_n.

$$\zeta = \cos\theta, \qquad (a15)$$

where θ is the angle between the particle velocity vector and the magnetic field line (see Fig. 30). The distribution function of the particles at the pellet surface is given by:

$$f_{e,i}(S_n, E, \zeta) = \left(\frac{E_{e,i0}(S_n, E, \zeta)}{E}\right)^{1/2} n_{e,i} \exp\left(\frac{-E_{e,i0}(S_n, E, \zeta)}{T_\alpha}\right)\left(\frac{L_{e,i}\left(E_{e,i\alpha0}(S_n, E, \zeta)\right)}{L_{e,i}(E)}\right),$$
$$(a16)$$

where $L_{e,i}(E)$ is the particle's loss function, $E_{e,i0}$ is the initial (at the neutral cloud boundary) energy of a particle. The loss function determines the energy losses of a particle:

21

$$\frac{dE}{dl} = -n_a(R)L_\alpha(E). \qquad (a17)$$

here – dl is the element of the particle's trajectory. We suppose that the particles loose their energy mainly on bound electrons in the cloud. Since an impurity pellet's atom has Z_p electrons (Z_p is a nuclear charge of pellet atoms), loss functions are taken equal to those for hydrogen, multiplied by Z_p. For electrons we have

$$L_e(E) = \frac{Z_p}{a_{e1} + a_{e2} \cdot E[eV]} \ [eV \cdot cm^2/atom], \qquad (a18)$$

where $a_{e1}=4.7 \cdot 10^{14}[atom/(eV \cdot cm^2)]$, $a_{e2}=8.0 \cdot 10^{11}[atom/(eV \cdot cm^2)]$, E is in eV. For ions

$$L_i(E) = Z_p \frac{1.93 \cdot 10^{-16}}{2} E[eV]^{0.4} \ [eV \cdot cm^2/atom]. \qquad (a19)$$

An integration (over the particle's trajectory in the cloud) of equation (a17) with loss function (a18), (a19) gives us the initial energy (at the neutral cloud boundary) of a particle as a function of the optical length of the cloud S_n and the particle's energy at the pellet surface – E:

$$E_{e0}(E_e, S_n, \xi) = -\frac{a_{e1}}{a_{e2}} + \sqrt{\left(E_e + \frac{a_{e1}}{a_{e2}}\right)^2 + \frac{2 \cdot Z_p S_n}{a_{e2}\xi}}, \qquad (a20)$$

$$E_{i0}(E_i, S_n, \xi) = \left(E_i^{0.6} + 0.6 \cdot \frac{1.93 \cdot 10^{-16}}{2} \frac{Z_p S_n}{\xi}\right)^{1.667}. \qquad (a21)$$

Substituting (a20) and (a21) into (a16) and then into (a13), we obtain (a12) – the heat flux density at the pellet surface as a function of the cloud optical length. $Q_{e,i}(0)$ is the heat flux density at the cloud boundary. Because of the charging effect at the cloud boundary the maxwellian heat flux densities are modified to $Q_e(0)=q_e/(2\pi r_p^2)$ and $Q_i(0) = q_i/(4\pi r_p^2)$, where q_e and q_i are determined by equations (a10) and (a11).

Cloud Gas Dynamics and Surface Averaging

The local ablation rate for different α should be calculated from the balance of the heat flux falling onto the pellet surface and the erosion heat flux. The heat flux penetrating to the pellet surface through a cloud with optical length S_n was discussed in the previous section. For the erosion heat flux we use the solution of the hydrodynamic equations obtained in [31]:

$$\frac{dr_p(\alpha)}{dt} = -0.52 \cdot \left(\frac{S_n}{r_p n_{as}}\right) \cdot \left[\frac{(Q_e(0)\cos\alpha + Q_i(0))(\gamma - 1)}{m_p S_n}\right]^{1/3}, \qquad (a22)$$

22

where γ is the ratio of specific heats for the cloud matter, n_{as} is the atomic density of the solid pellet's material, m_p is the pellet's atom mass.

This equation expresses the relation between the thermal fluxes at the neutral cloud boundary ($S_n=0$) (which determines the cloud expansion energy), the cloud optical length and the ablation rate.

The balance of 1) the heat flux penetrating to the pellet surface through the cloud with optical length S_n (a12) and 2) the heat flux, evaporating the pellet surface, appropriate to create a cloud with such length (a22), can be expressed as follows:

$$-\lambda n_{as} \frac{dr_p(\alpha)}{dt} = Q_e\left(\frac{S_n}{cos\,\alpha}\right)cos\,\alpha + Q_i(S_n). \qquad (a23)$$

Here λ is the sublimation energy of the pellet material plus enthalpy of the solid-gas phase transition (for lithium $\lambda \approx 2.1$ eV/atom). This balance determines the local cloud optical length $S_{na}(\alpha)$ and also the local ablation rate, which is equal to

$$\frac{d\dot{N}}{ds} = n_{as}\,2\pi r_p^2\,\frac{dr_p(\alpha)}{dt}sin(\alpha)d\alpha \qquad (a24)$$

for a spherical pellet. Here ds is the element of pellet surface.

The total ablation rate in this case is

$$\dot{N} = 2\pi r_p^2 \cdot 2 \int_{\alpha=0}^{\frac{\pi}{2}} n_{as}\frac{dr_p(\alpha)}{dt}sin(\alpha)d\alpha. \qquad (a25)$$

Self-limiting of ablation

Equation (a25) determines the ablation rate of a spherical pellet with radius r_p in an infinite homogeneous maxwellian plasma with density n_e, electron temperature T_e and ion temperature T_i in quasi-steady state. In real pellet injection experiments the ablating pellet influences the plasma parameters so that the temperature and density profiles modify during the ablation process. This effect is called ablation self-limiting and can be considered in collisionless [32] or adiabatic [16] approach.

In the collisionless approach the possible depletion of electron population when the pellet moves towards the plasma centre is given by the model of Houlberg et al. [32]. As a result, the effective electron heat flux, flowing onto the pellet from the bulk plasma, reduces to

$$Q_{ed} = Q_e \frac{\tau_d}{\tau_{p0}} \left(1 - e^{-\tau_{p0}/\tau_d} \right), \quad \tau_d = \frac{\Delta V}{v_{par}\left(2\pi r_i^2\right)}, \quad \tau_{p0} = \frac{2r_i}{v_p} \qquad (a26)$$

where $Q_e = n_e \sqrt{\dfrac{2T_e^3}{\pi m_e}}$ is the undisturbed electron heat flux density, τ_d is the characteristic time of heat flux density depletion, ΔV is the volume of the magnetic tube containing the pellet cloud, v_{par} is the electron velocity along the magnetic field, v_p is the pellet velocity transverse to the magnetic field, r_i is an adjusting parameter which has the meaning of the neutral cloud radius.

When the pellet passes the plasma centre it faces with plasma which could be cooled by previously deposited ablatant, a case of adiabatic self-limiting takes place. The algorithm of this self-limiting phenomenon for Li pellet ablation studies in Heliotron E machine is described in Ref. [16]. In our simulations we consider that at each magnetic surface the electron pressure $n_e T_e$ remains constant during the ablation process.

The algorithm of ablation rate calculation

We divide the pellet trajectory into a number of small intervals over which the plasma parameters (n_e, T_e, T_i) can be considered homogeneous. At each step the heat flux balance (a23) is solved for different α-angles, the local ablating heat flux $Q(S_n, \alpha)$ (a12), the local ablation rate (a24) and the total ablation rate (a25) are found. With the help of this value of the ablation rate the pellet radius at the next step is found, which allows us to find the ablation rate at the next step, etc. On the first half of the pellet trajectory (towards the plasma centre) the ablation rate (a25) is calculated for undisturbed temperature profiles. The heat flux profile is modified according to (a26) in collisionless self-limiting approach. On the second half of the pellet trajectory (after the magnetic axis) both self-limiting mechanisms are taken into account.

Simulation of pellet ablation by charged pellet model

To verify the described model we simulated ablation rate profile of the Li pellet 1x∅1 mm in size injected with velocity 450 – 500 m/s into ECR-heated plasma of the Heliotron E machine [16]. The results of simulations are shown in Fig. 31. Here, dashed curve – experimental ablation rate deduced from the Li^{+1} cloud emission, solid line – simulated ablation rate. We see that the model fairly good predicts the ablation rate behaviour except the zone between minor radii 5 – 15 cm where enhanced ablation could

be caused by suprathermals as it was supposed in [16]. It should be noted that similar behaviour of ablation (enhanced ablation) of carbon pellets injected into ECR-heated plasma has been observed on W7-AS [33].

In Fig. 32 the ablation rate profiles of a carbon pellet in shot # 43561 in W7-AS ECR-heated plasma are shown. The dotted curve corresponds to the experimental ablation rate deduced from the C^{II} cloud emission, solid curves show the simulated ablation rate. Enhancement of the measured pellet ablation rate at effective minor radii 8-12 cm (possibly due to supra-thermal electrons) cannot be described by the model and the experimental ablation rate values are taken for this part with a goal to perform further simulations at 2-8 cm. Thick solid curve is the simulation by the model, where the effect of electron heat flux depletion near the magnetic axis is taken into account. Thin solid curve is the simulation by the model without the effect of depletion. It can be seen from Fig. 31 and Fig. 32 that the model which takes into account the depletion of the electron heat flux allows to describe the reduction of the ablation rate near the plasma axis if an adjusting parameter r_i in eq. (a26) is chosen properly: For Heliotron-E $r_i = 0.2$ cm and for W7-AS $r_i = 0.2$ cm.

References

[1] J.E. Bayfield, Phys. Rev. **185** (1969) 105.

[2] A.A. Korotkov, A. Gondhalekar and A.J. Stuart Nucl. Fusion **37** (1997) 35.

[3] S.S. Medley, D.K. Mansfield, A.L. Roquemore *et al.* Rev. Sci. Instrum. **67** (1996) 3122.

[4] S.S. Medley, R.K. Fisher, A.V. Khudoleev *et al.*, Proc. 20th EPS Conference on Contr. Fusion and Plasma Physics, Lisbon, 1993, Vol. 17C p.III-1183

[5] J.M. McChesney, H.H. Duong, R.K. Fisher *et al.* Rev. Sci. Instrum. **66** (1995) 348.

[6] H.H. Duong, R.K. Fisher, J.M. McChesney *et al.*, PPPL-3192 (May, 1996)

[7] M.P. Petrov, R.V. Budny, H.H. Duong *et al.* Nucl. Fusion **35** (1995) 1437.

[8] M.P. Petrov, N.N. Gorelenkov, H.H. Duong *et al.*, Proc. 23[d] EPS Conference on Contr. Fusion and Plasma Physics, Kiev, 1996, report a012, vol I, p.63.

[9] H.H. Duong, R.K. Fisher, J.M. McChesney *et al.*, Rev. Sci. Instrum. **68(1)** (1997) 340.

[10] M.P. Petrov, N.N. Gorelenkov, R.V. Budny *et al.*, 16th IAEA Fusion Energy Conference, Montreal, 1996, IAEA-CN-64/A2-2 paper

[11] S.S. Medley, R.V. Budny, H.H. Duong, *et al.*, Nuclear Fusion **38** (1998) 1283

[12] J.M. McChesney, P.B. Parks, R.K. Fisher *et al.*, Phys. Plasmas **4** (1997) 381

[13] M.P. Petrov, R. Bell, R.V. Budny *et al.* Physics of Plasmas **6** (1999) 2430.

[14] B.V. Kuteev, A.Yu. Kostrukov, L.R. Baylor, G.Schmidt sumbitted to Nuclear Fusion.

[15] H. Wobig, Plasma Parameters in Wendelstein 7-X, Ringberg Workshop, 1995.

[16] V. Yu. Sergeev *et al.*, Plasma Phys. Control. Fusion **40** (1998) 1785.

[17] G. W. Barnes, R. C. Gemhardt, D. Mansfield. Book of Abstracts of Symposium on Fusion Engineering, (1995), Abstract 0605, p.176.

[18] K. V. Khlopenkov, S. Sudo, V. Yu. Sergeev. Report, NIFS-TECH-4, May 1996, Nagoya.

[19] Terry *et al.,* Rev. Sci. Instrum **62** (1990) 2908

[20] D. H. McNeil, et. al., Spectroscopic measurements of the parameters of the ablation clouds of deuterium pellets injected into tokamaks, Phys. Fluids B 3 (1991) 1994-2009.

[21] K.L. Bell, *et.al.*, J. Phys. Chem. Ref. Data, Vol. 12, No. 4, (1983), pp. 891-916.

[22] A. Howald, private communication

[23] S.L. Milora, New Algorithm for Computing the Ablation of Hydrogenic Pellets in Hot Plasma, Oak Ridge National Laboratory Rep. ORNL/TM-8616 (1983)

[24] J. D. Jackson, Classical Electrodynamics (Wiley, New York, 1974), Chap.13.

[25] J.A. Snipes *et al.* J. Nucl. Materials **196-198** (1992) 686.

[26] K.V. Khlopenkov, S. Sudo, NIFS-TECH-4 report, Nagoya, May 1996

[27] J. Junker, A. Weller IPP 2/341 (1998).

[28] V. Erckmann, H.J. Hartfuss, M. Kick *et al.*, 17th IEEE/NPSS Symposium on Fusion Engineering, San Diego, October 6 –10, 1997, pp. 40-48.

[29] T.H. Stix, Nuclear Fusion **15** (1975) 737.

[30] J.G. Laframbouise Report No. 100, Inst. for Airospace Studies, Univ. of Toronto, Toronto (1966).

[31] B.V. Kuteev *et al.* Fusion Technology, **26** (1994) 938.

[32] W.A. Houlberg *et. al.* Nuclear Fusion **28** (1988) 595.

[33] L. Ledl *et. al.* Proc. 26th EPS Conference on Contr. Fusion and Plasma Phys., 14-18 June, Maastrict, ECA 23J (1999) 1477-1470

[34] Rozhanskii V.A. Sov. Journal of Plasma physics, **15** (1989) 1101.

Table 1.

$n_e(0)$ (10^{13})cm^{-3}	$T_e(0)$ (keV)	τ_{sl} (s)	T_{Stix} (keV)
1	10	4.0	4500
2	9	1.7	950
3	8	0.95	370
4	7	0.58	170
5	6	0.37	86
6	6	0.3	58
7	5	0.2	34
8	4.5	0.15	22
9	4	0.11	15
10	4	0.1	11
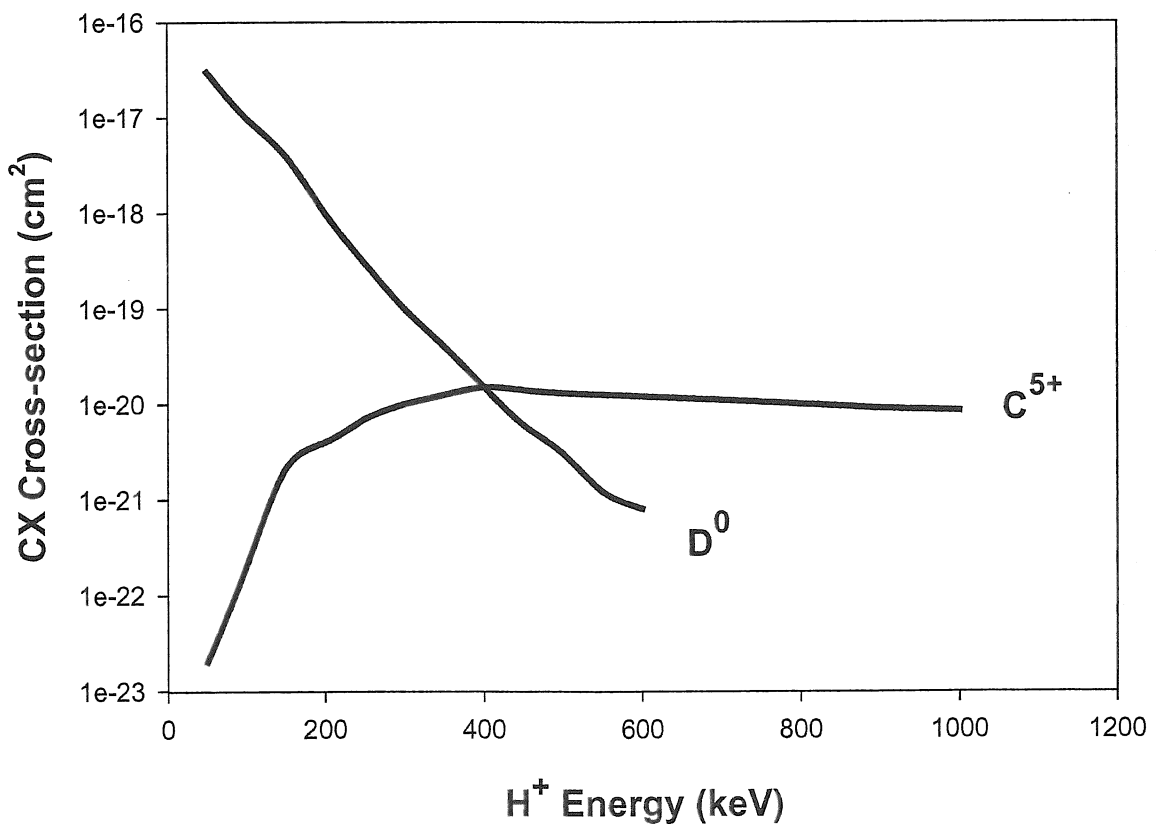
Fig. 1. Cross sections for proton charge exchange with D^0 atoms and with C^{5+} ions.
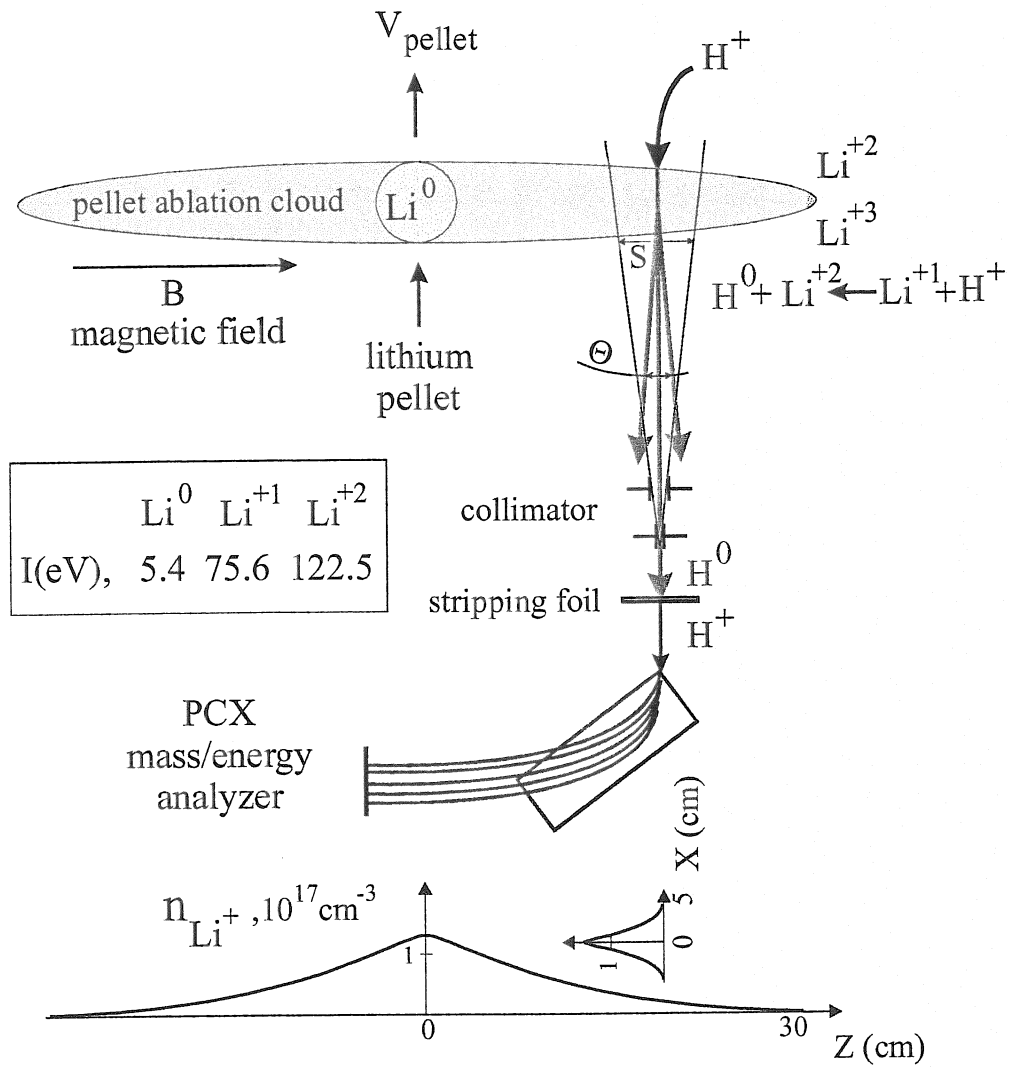
Fig. 2. Principal scheme of PCX diagnostic.
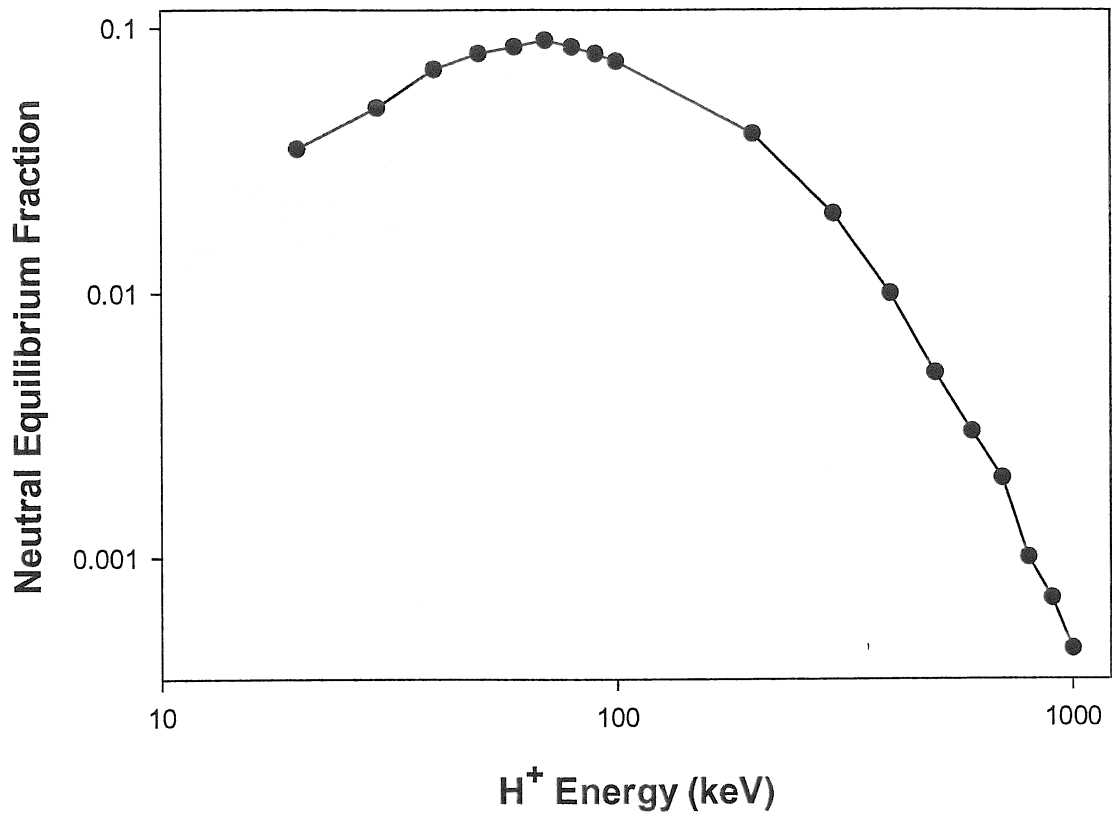
Fig. 3. Equilibrium fraction of protons that emerge as neutrals from a Li^+ target.
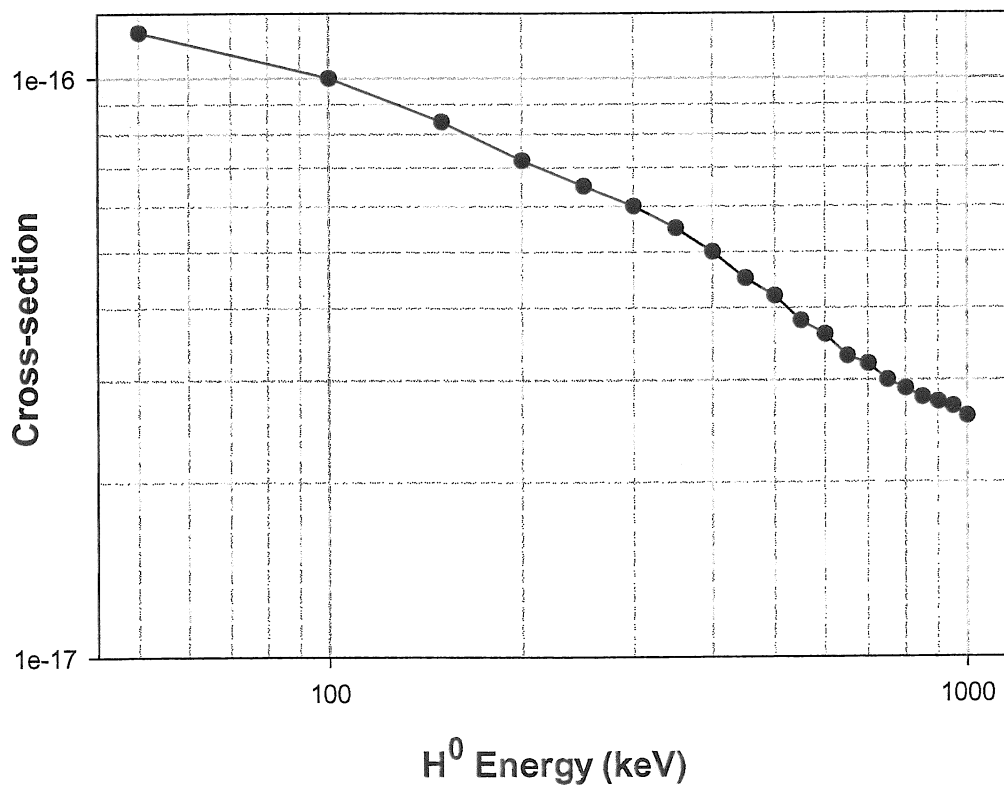
Fig. 4. H^0 stopping cross-section in D plasma.
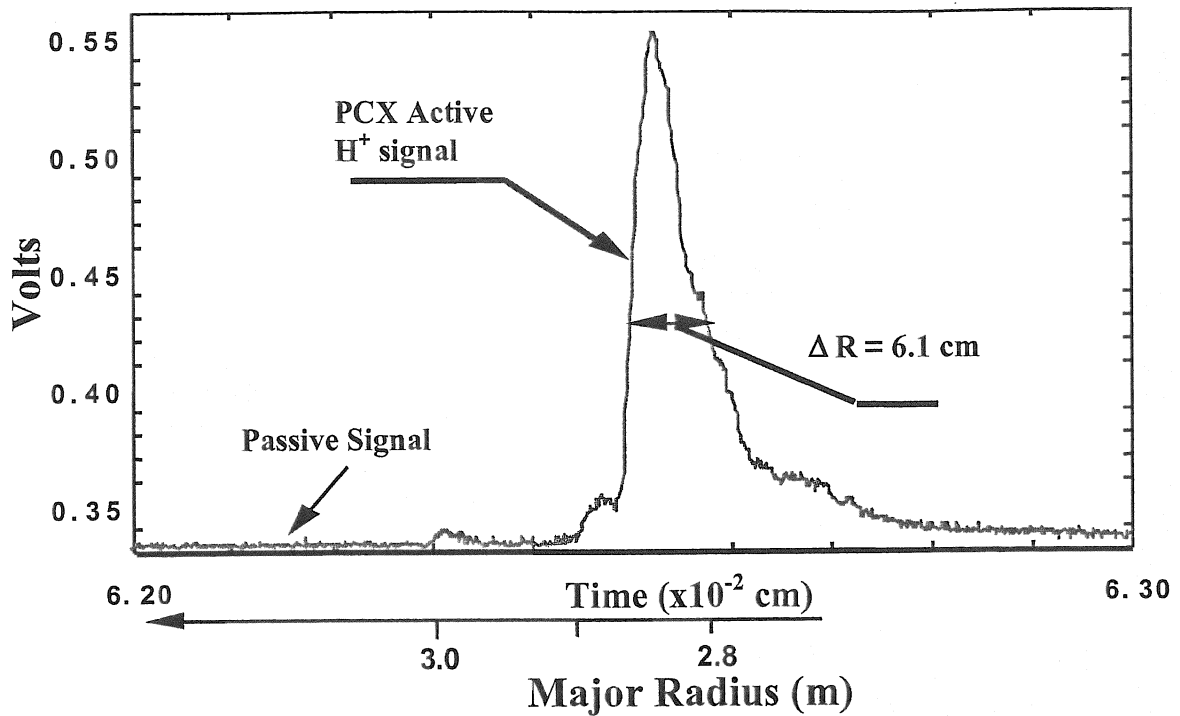
Fig. 5. Radial position and shape of the H^+ (E=0.72MeV) resonance measured by PCX active diagnostic for fundamental H^+ ICRF heating in a TFTR deuterium plasma.
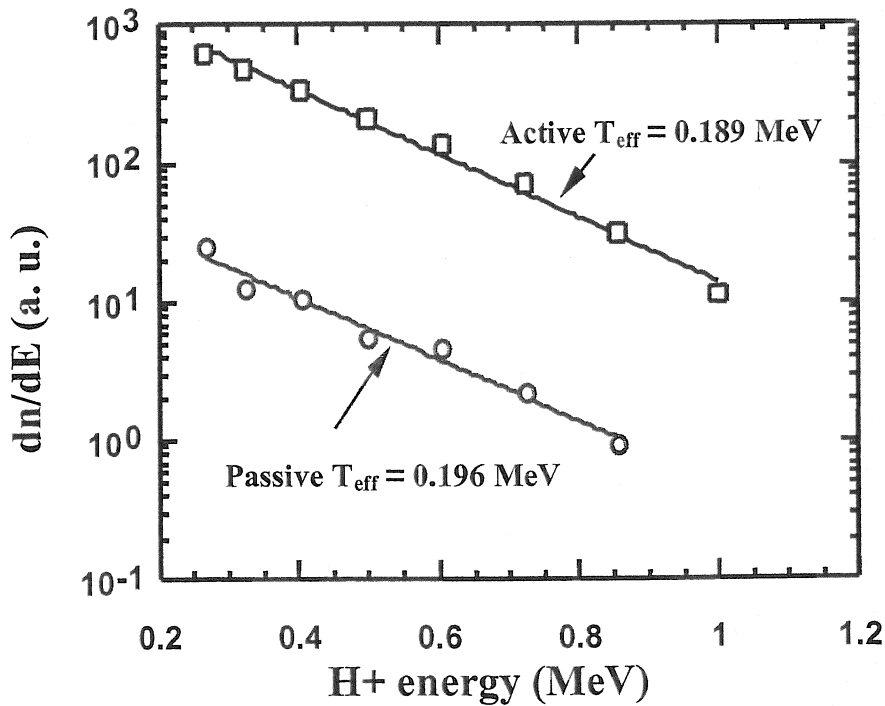
Fig. 6. Active and passive energy spectra of H^+ ICRF driven minority ions in a TFTR deuterium plasma are in close agreement. Both discharges were obtained with on-axis heating at P_{ICRF} = 2.1 MW, F = 43 MHz, $N_e(0)$ = 5·10^{13} cm^{-3} [13].

PI – Li pellet injector,

NPA – neutral particle analyser,

WVD – wide view detector,

CPA – collimated photodiode array,

CAM1,2 – CCD cameras.
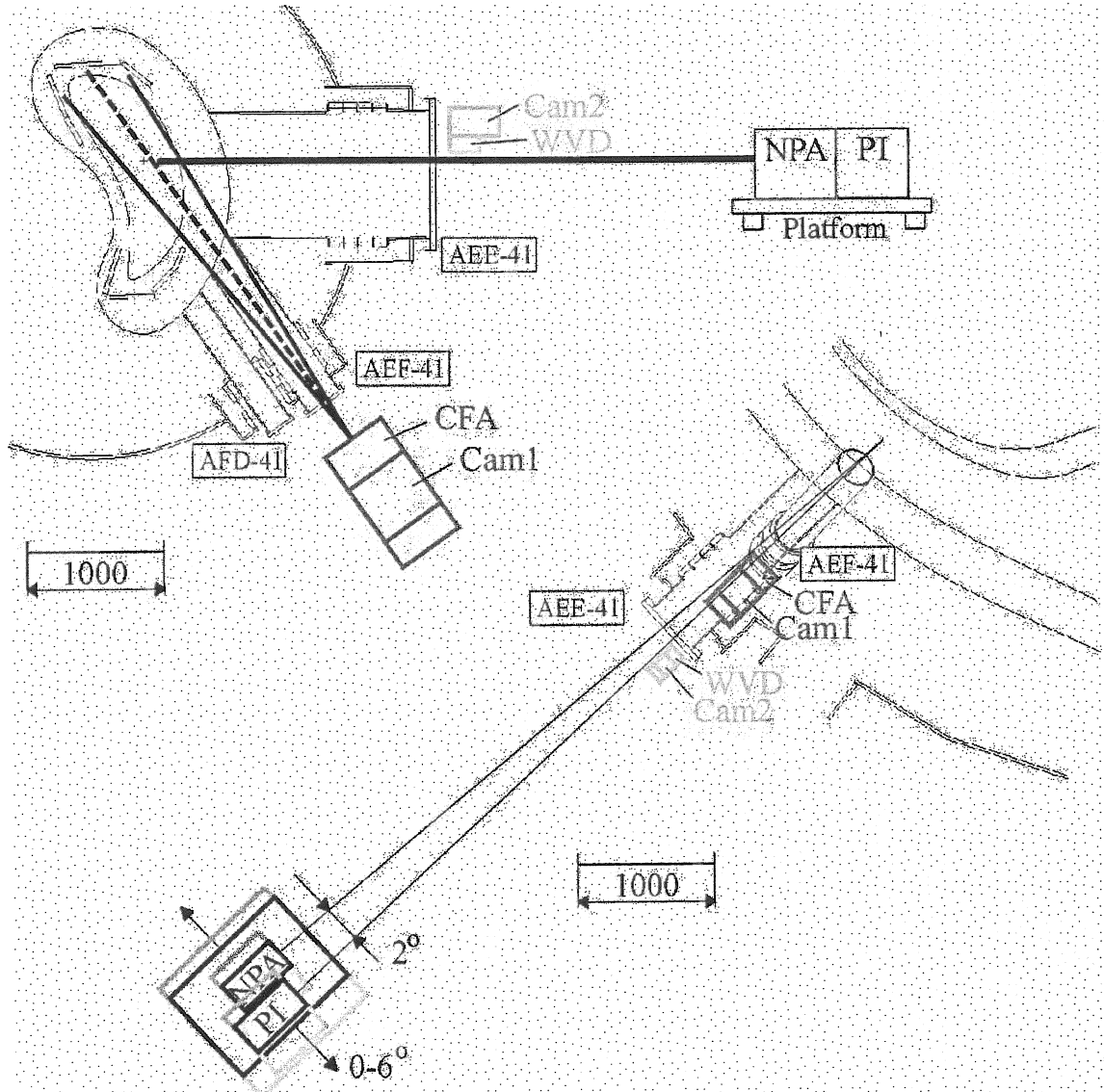
Fig. 7. PCX experimental setup proposed for W7-X: a) poloidal, b) top-of view.
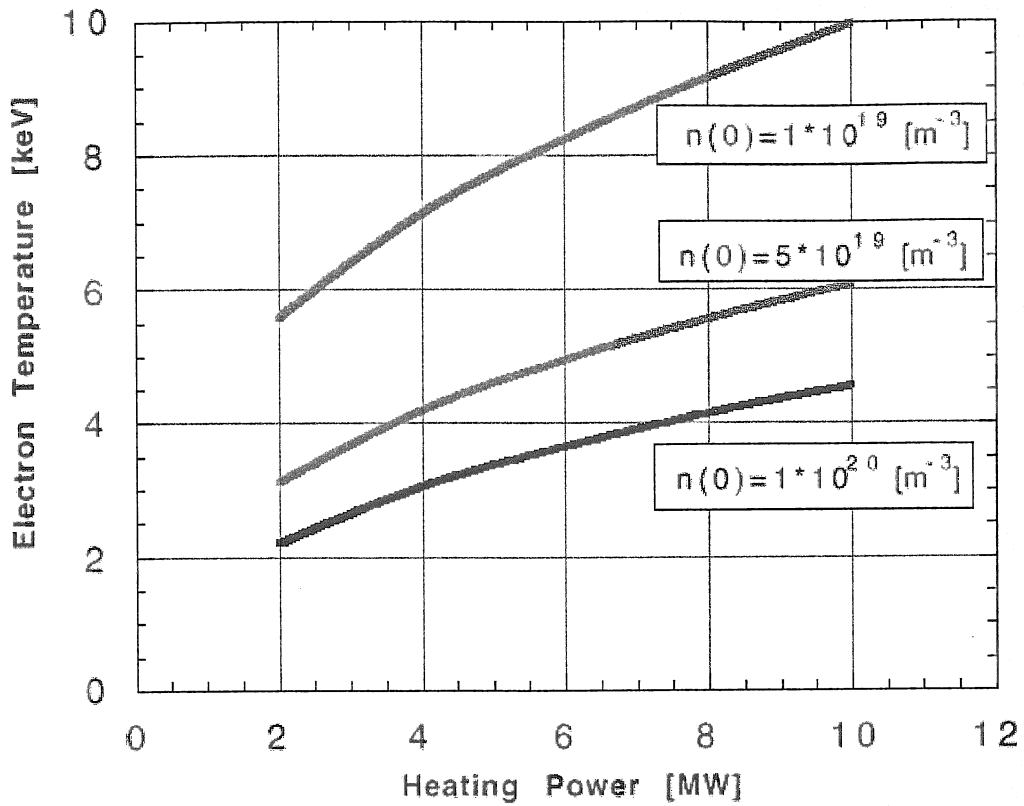
Fig. 8. Peak electron temperature in ECR-heated W7-X plasmas. R = 5.5 m, B = 2.5 T.
Results of TEMPL code from Ref. [15]. Density profile r_n = 0.73, α_n = 3.0.
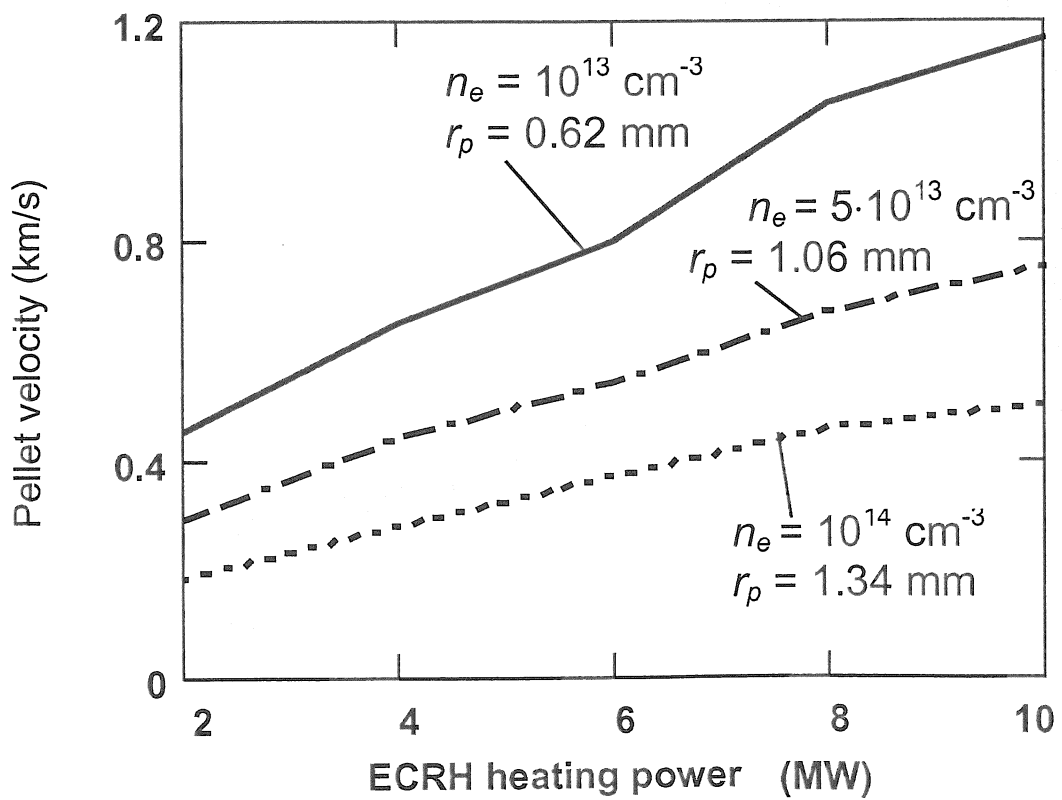
Fig. 9. Li pellet velocity for W7-X plasma core penetration.
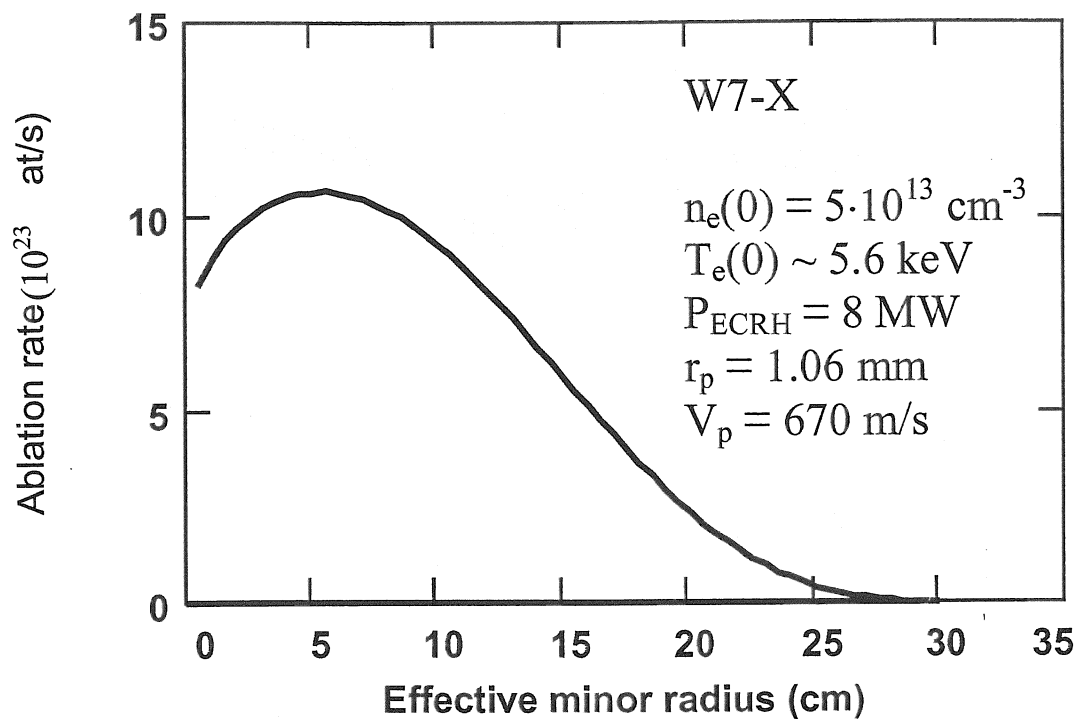
Fig. 10. Calculated typical Li pellet ablation rate in W7-X.

$$n_e(0) = 5 \cdot 10^{13} \text{ cm}^{-3}$$
$$T_e(0) \sim 5.6 \text{ keV}$$
$$P_{ECRH} = 8 \text{ MW}$$
$$r_p = 1.06 \text{ mm}$$
$$V_p = 670 \text{ m/s}$$
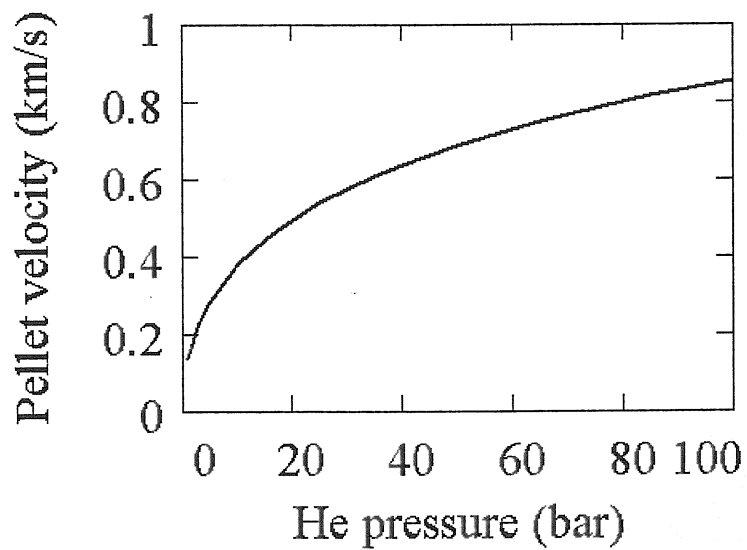
Fig. 11. The dependence of Li pellet velocities on the propellant (He) gas pressure for one-stage light gas–gan with barrel length 120 mm and diameter 2.5 mm.
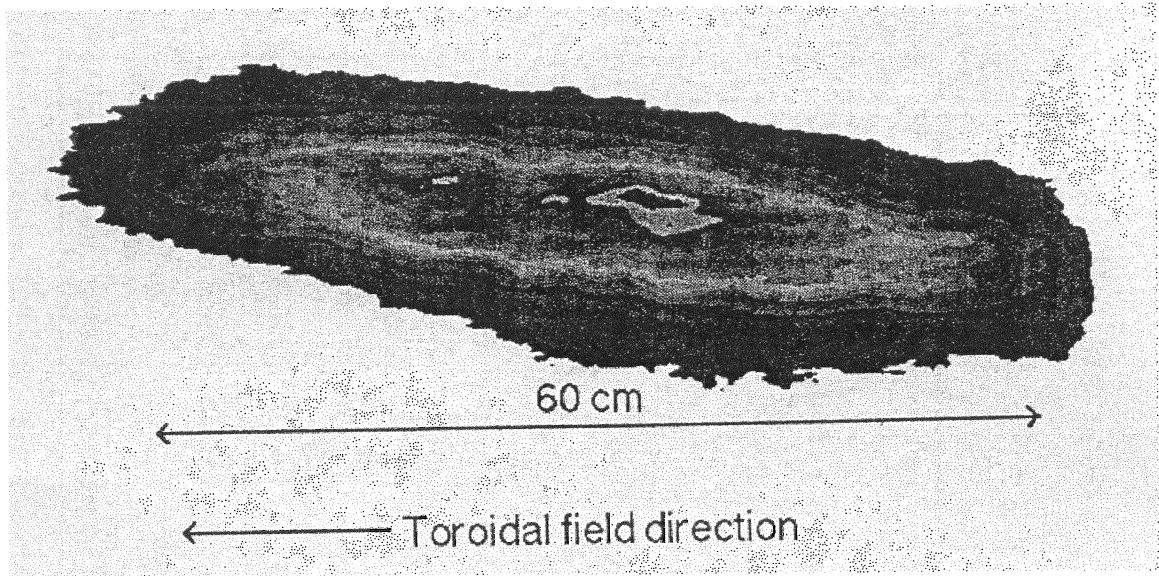
Fig. 12. Li$^+$ cloud imaged through a 548.5nm line filter in TFTR #52197
(pellet viewed from behind).
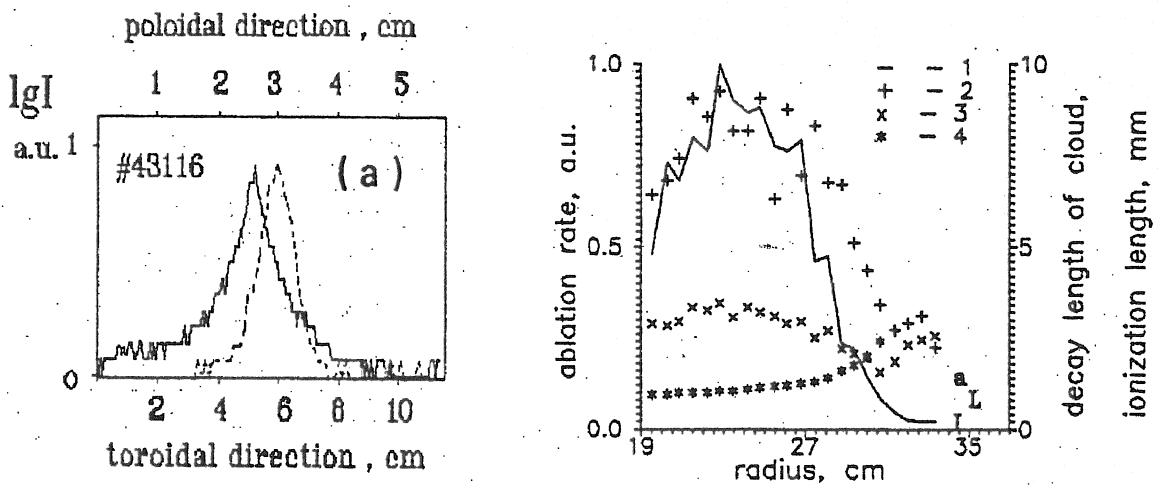
Fig. 13. T-10 carbon pellet experiments
($a = 17.5$ cm, $T_{e0} = 0.75$ keV, $n_{e0} = 10^{13}$ cm^{-3}, $r_p = 0.17$ mm).
a) Poloidal (dashed curve) and toroidal (solid curve) distributions of cloud luminosity
derived of a snap-shot (40 μs exposure time, total visible range of light $\Delta\lambda = 400$-600nm).
b) The pellet ablation rate, the decay lengths and the ionisation length versus minor plasma
radius in Shot #43196. 1 - ablation rate, 2 – toroidal length, 3 – poloidal length, 4 -
ionisation length.
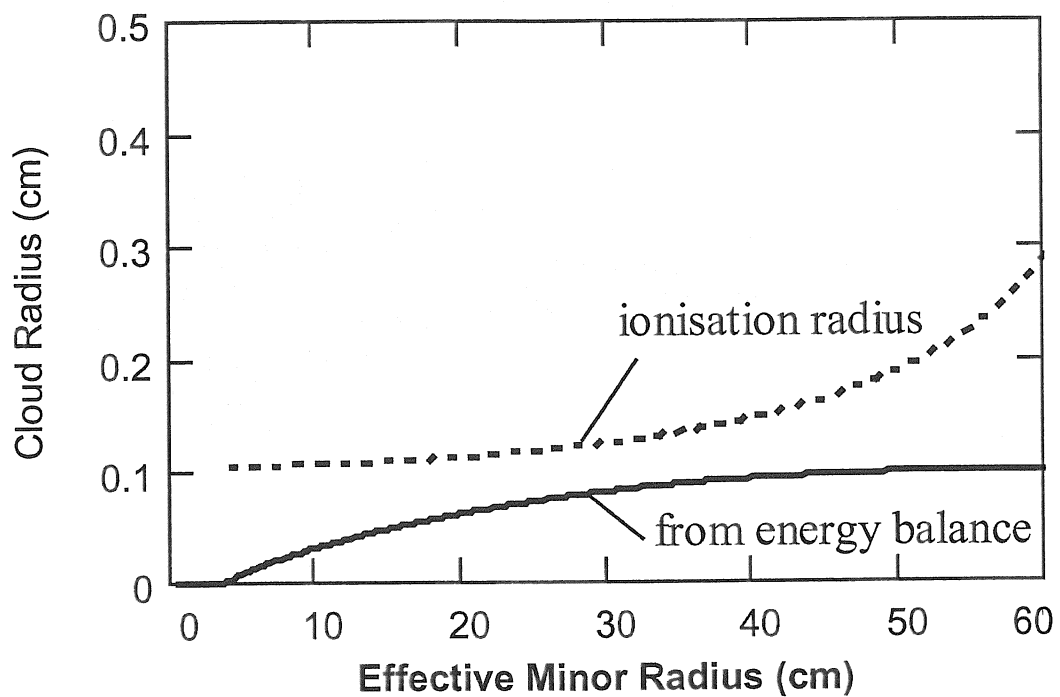
Fig. 14. Li$^+$ cloud radius in TFTR #52197.
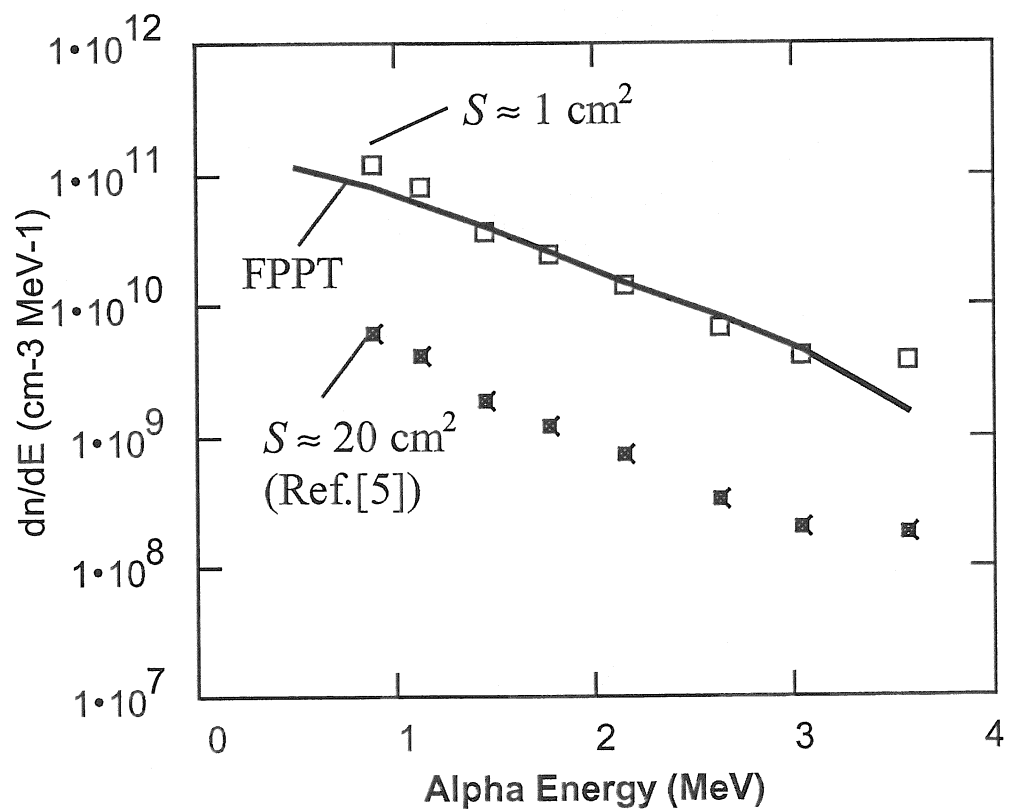
Fig. 15. Comparison between experimental and calculated
alpha energy distribution function in TFTR #86291.

35

a) $r_{cl} \geq r_{NPA}$ b) $r_{cl} \ll r_{NPA}$

Fig. 16. Possible disposition of a pellet cloud and the area visible to the NPA.
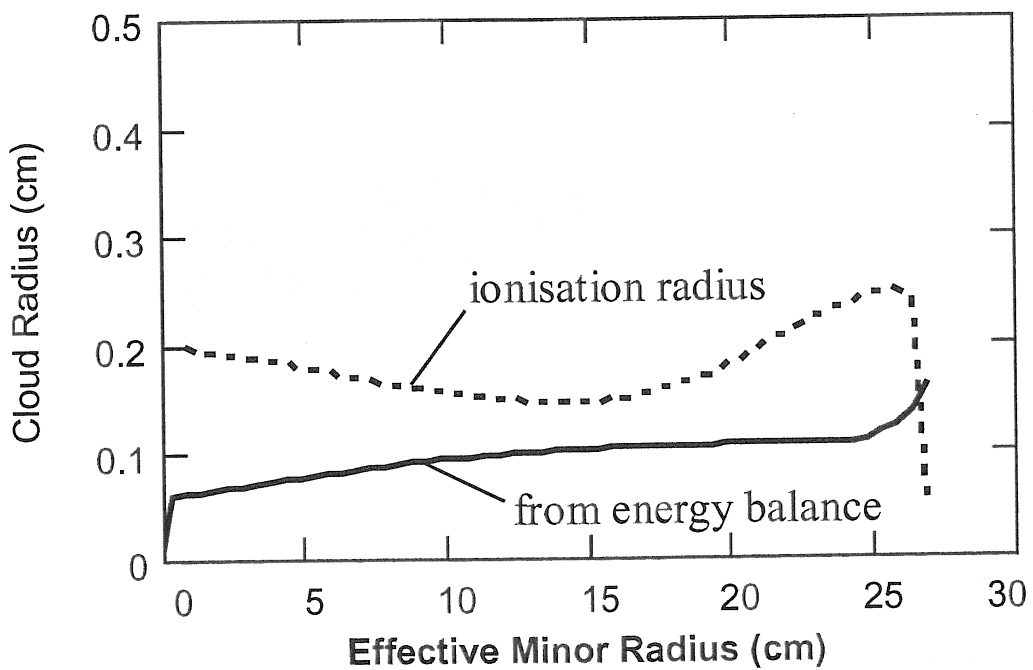
Fig. 17. Li$^+$ cloud radius for expected typical pellet ($\varnothing 2.1$mm) ablation in W7-X.
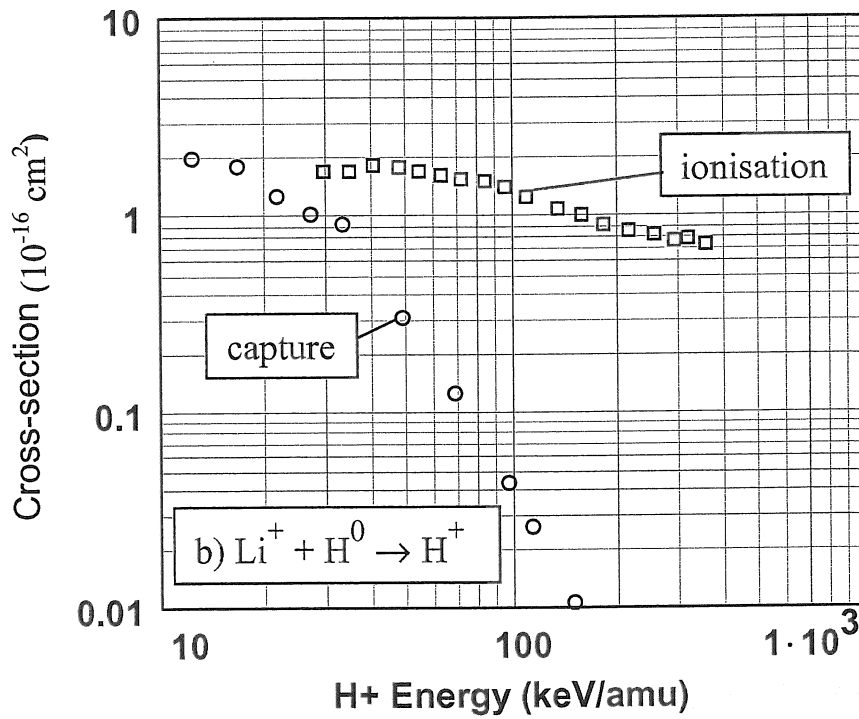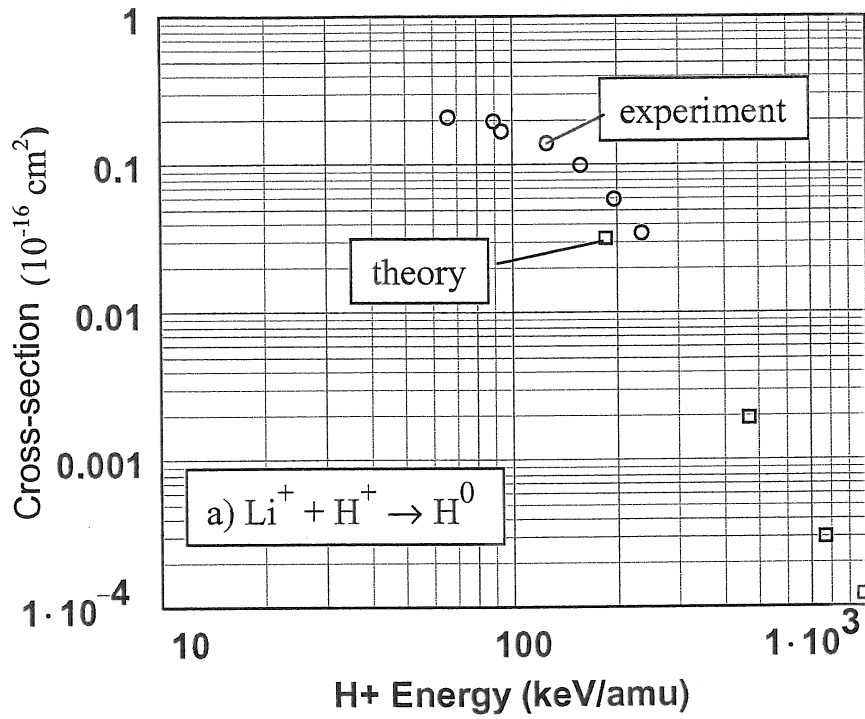
Fig. 18. Cross-sections of charge exchange of protons in Li^+ cloud:
a) $H^+ \rightarrow H^0$, b) a) $H^0 \rightarrow H^+$ (capture, ionisation)
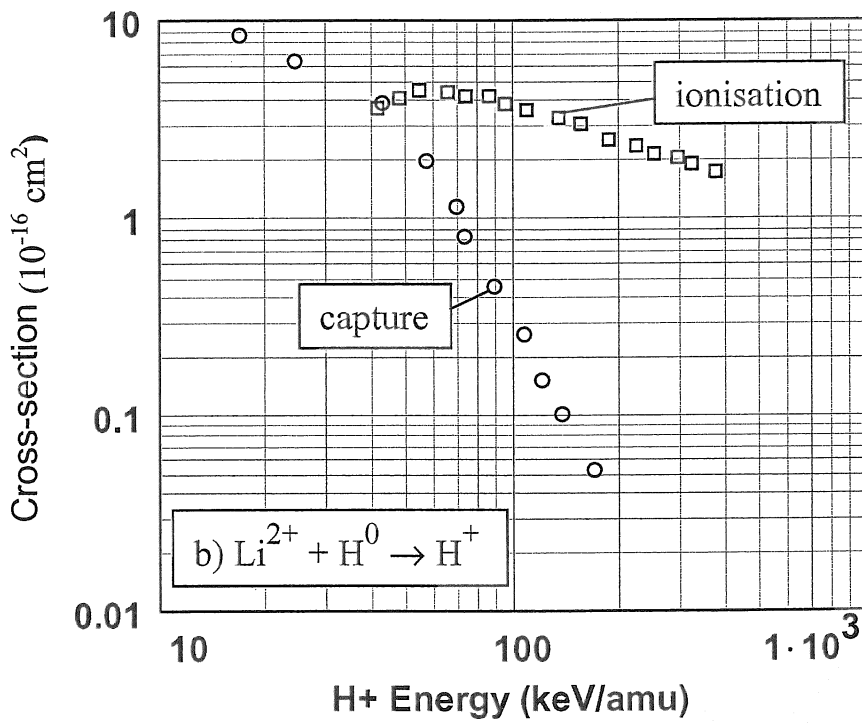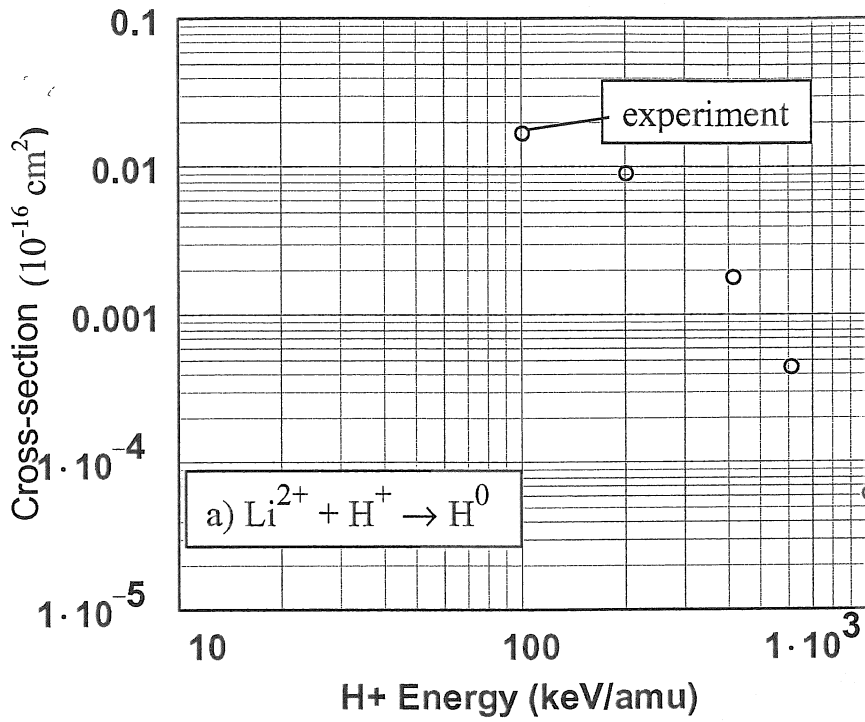
Fig. 19. Cross-sections of charge exchange of protons in Li^{2+} cloud: a) $H^+ \rightarrow H^0$, b) a) $H^0 \rightarrow H^+$ (capture, ionisation)
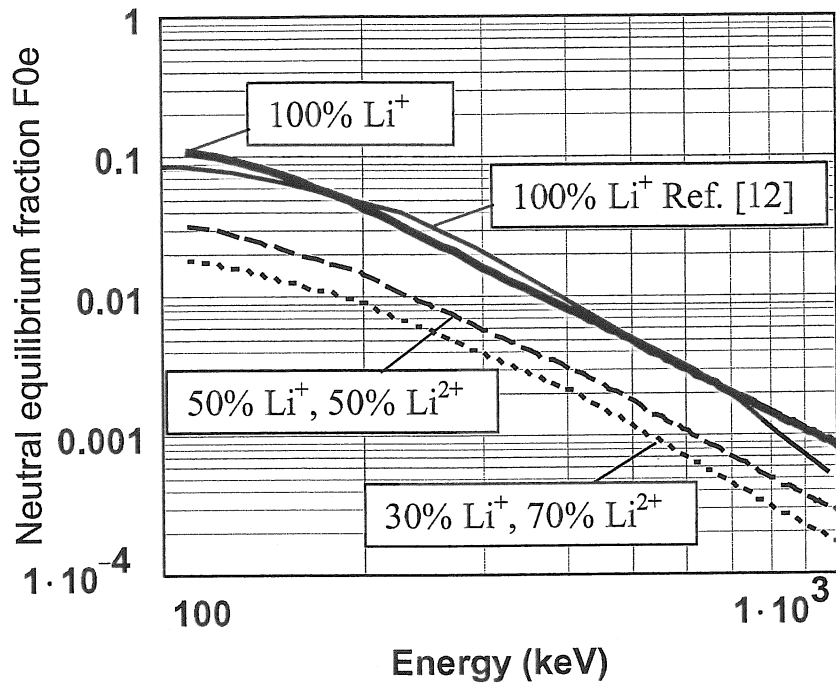
Fig. 20. Equilibrium neutral fraction of H^0 for different Li cloud charge state compositions.
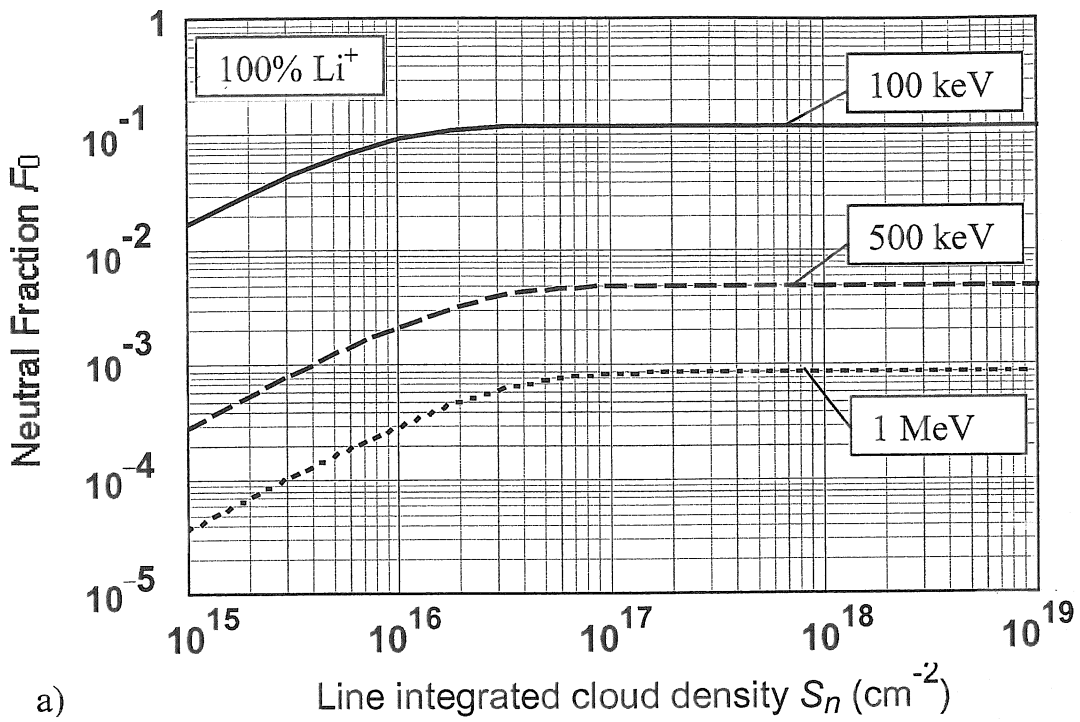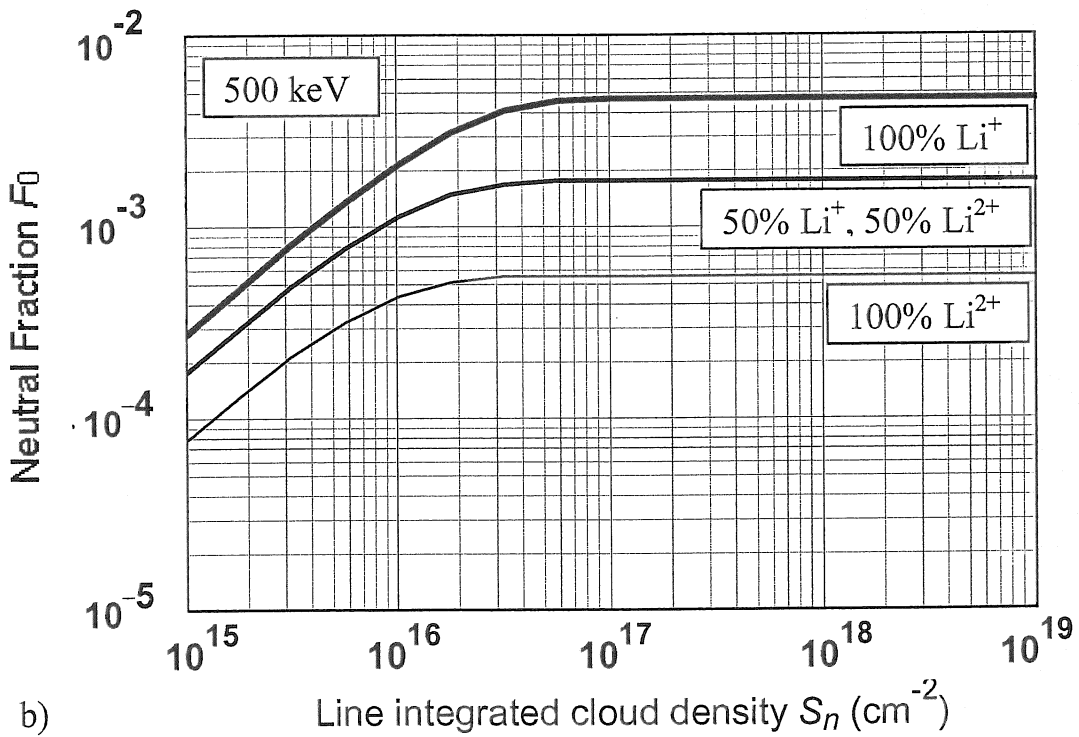
Fig. 21. The fraction of protons emerging as neutrals from Li^+ cloud
versus line integral cloud density for different H^0 energies.
a) in 100% Li^+ cloud for proton energy 100 keV, 500 keV, 1 MeV
b) for proton energy 500 keV in 100% Li^+, 50% Li^+ 50% Li^{2+} and 100% Li^{2+} cloud.
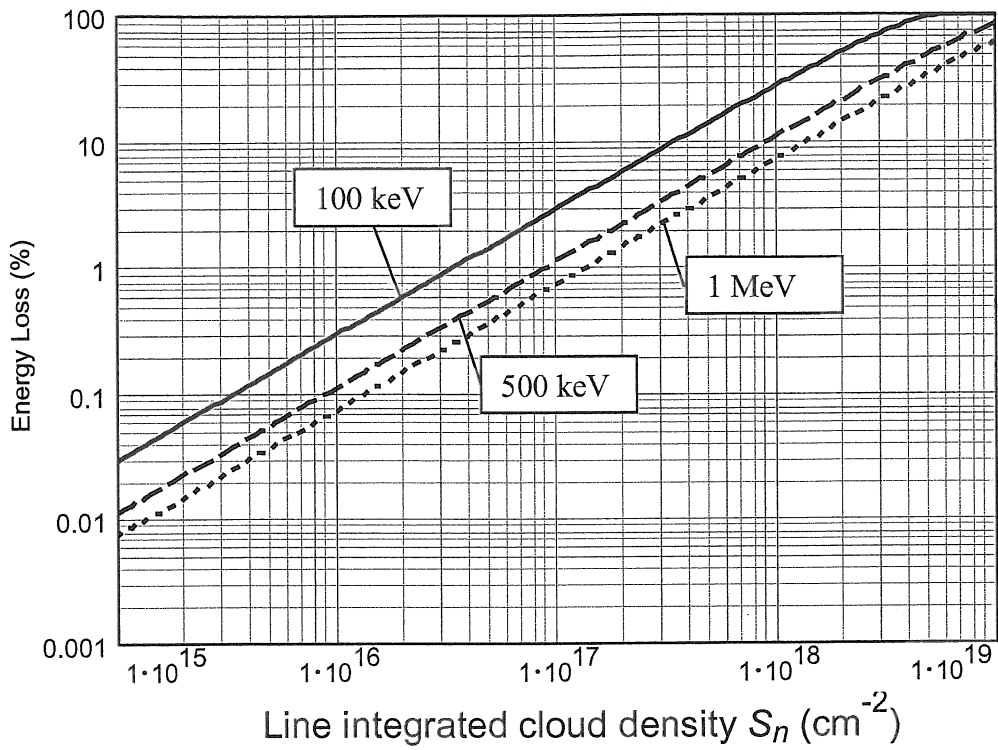
Fig. 22. Relative energy loss of fast protons in Li$^+$ cloud.
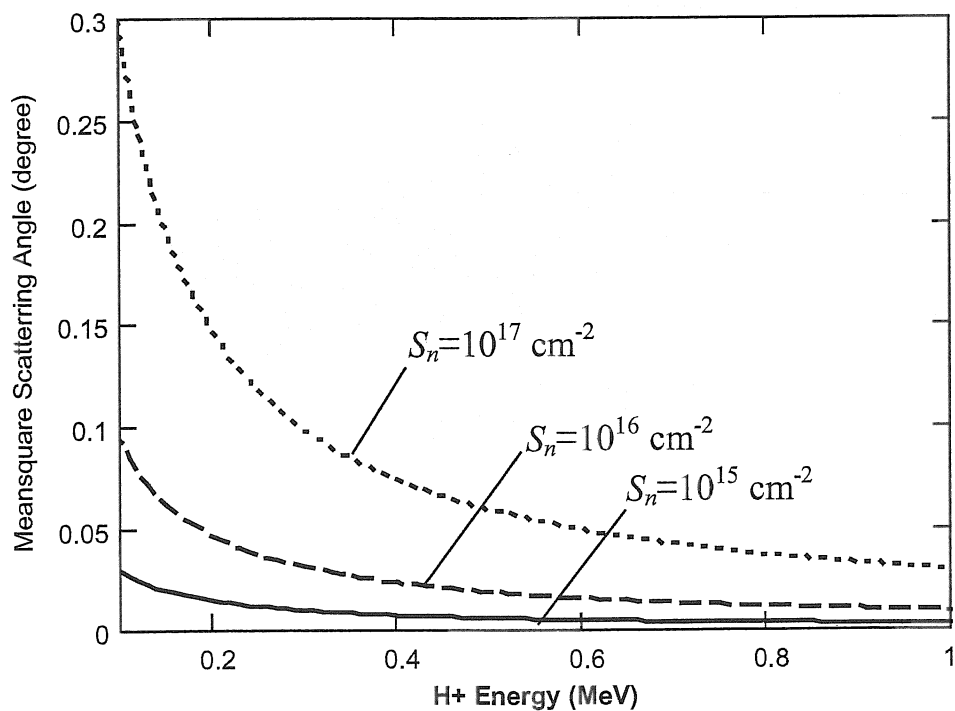
Fig. 23. Meansquare angular deviation of fast protons in Li$^+$ cloud.
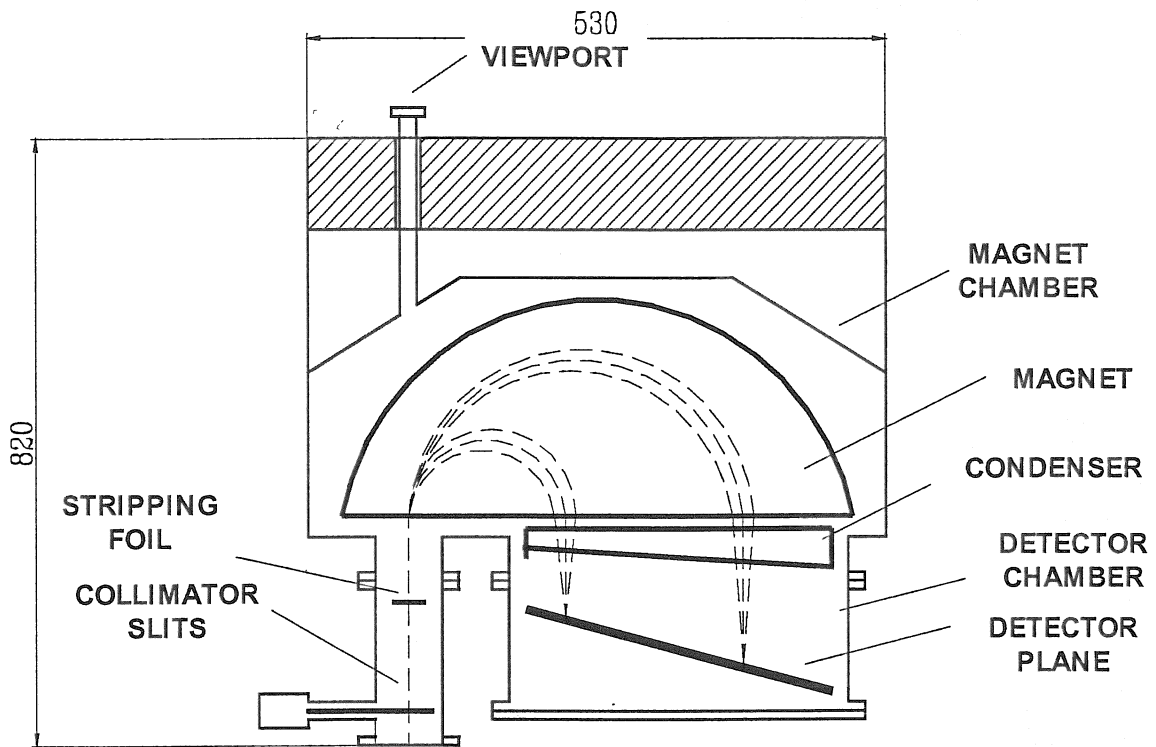
Fig. 24. The schematic of the Neutral Particle Analizer (NPA) ISEP-2.
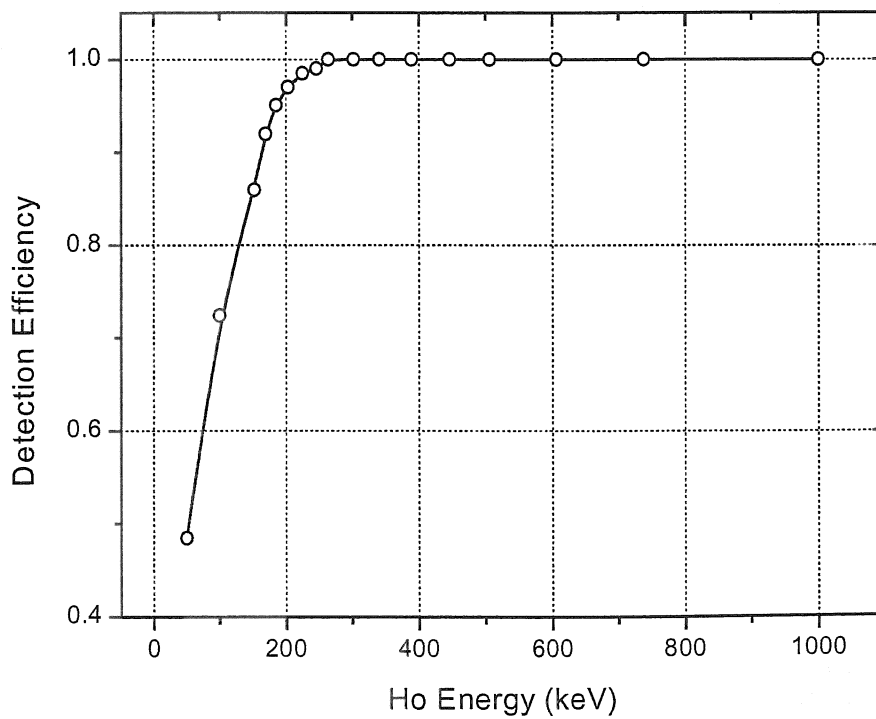
Fig. 25. NPA ISEP detection efficiency for H^+ ions. Stripping in carbon foil (300 A)
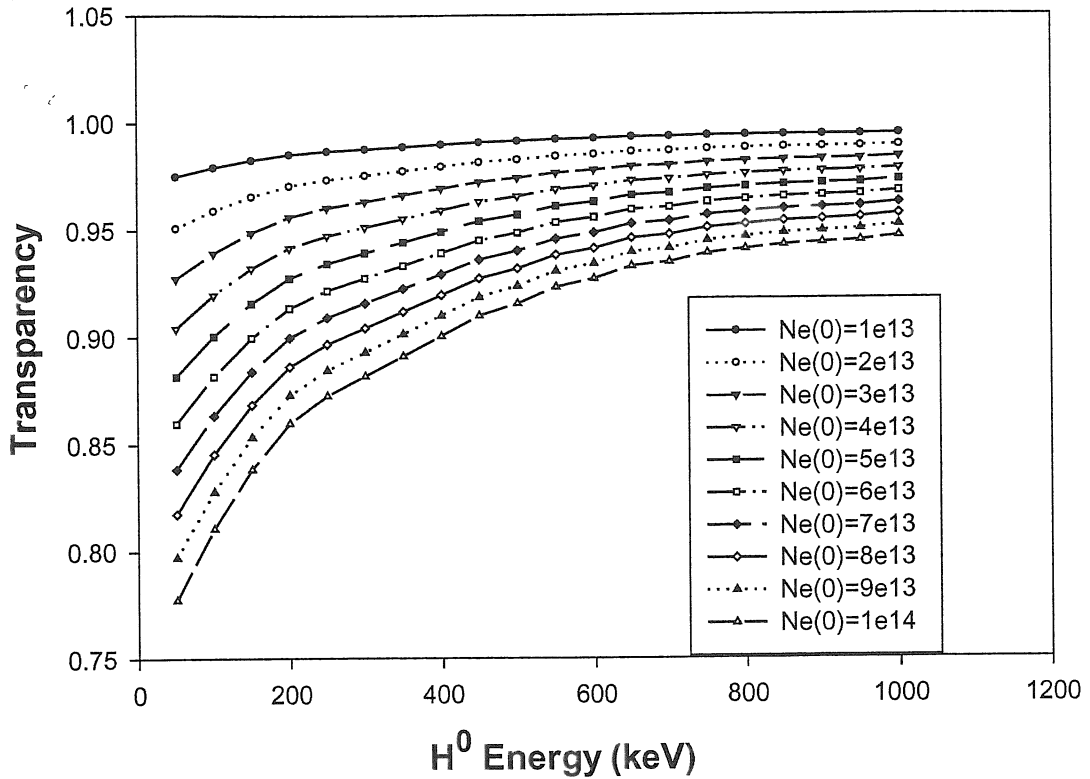
Fig. 26. W7-X Plasma Transparency for H^0 atoms vs Energy
in the Density Range 10^{13} - 10^{14} cm^{-3}.
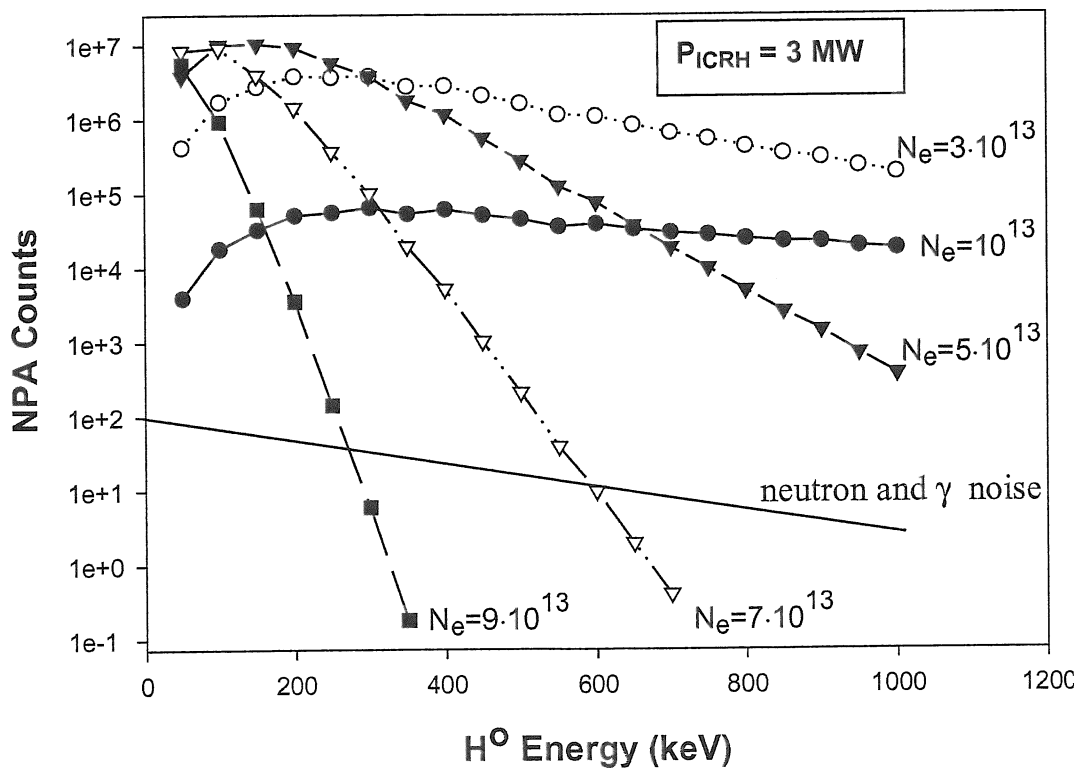
Fig. 27. Calculated NPA counts of H^0 atoms at the NPA in PCX diagnostic vs. Energy
for W7-X RF minority - heated plasma (P_{RF}=3 MW) in the density range 10^{13}-$9 \cdot 10^{13}$ cm^{-3}.
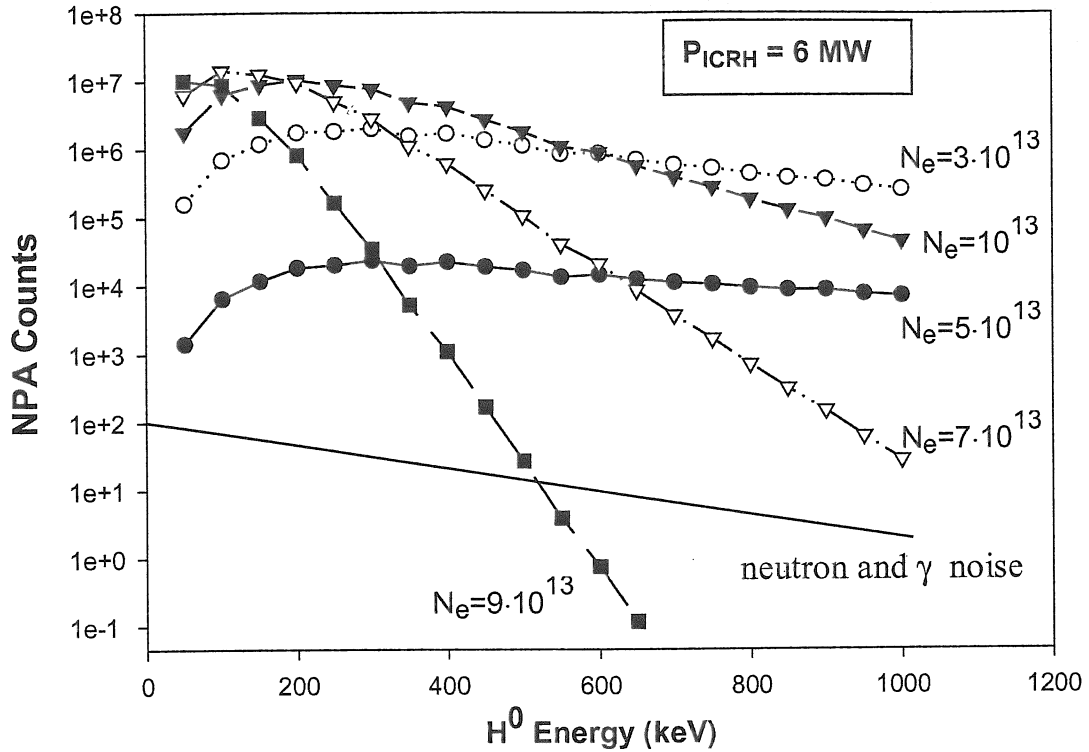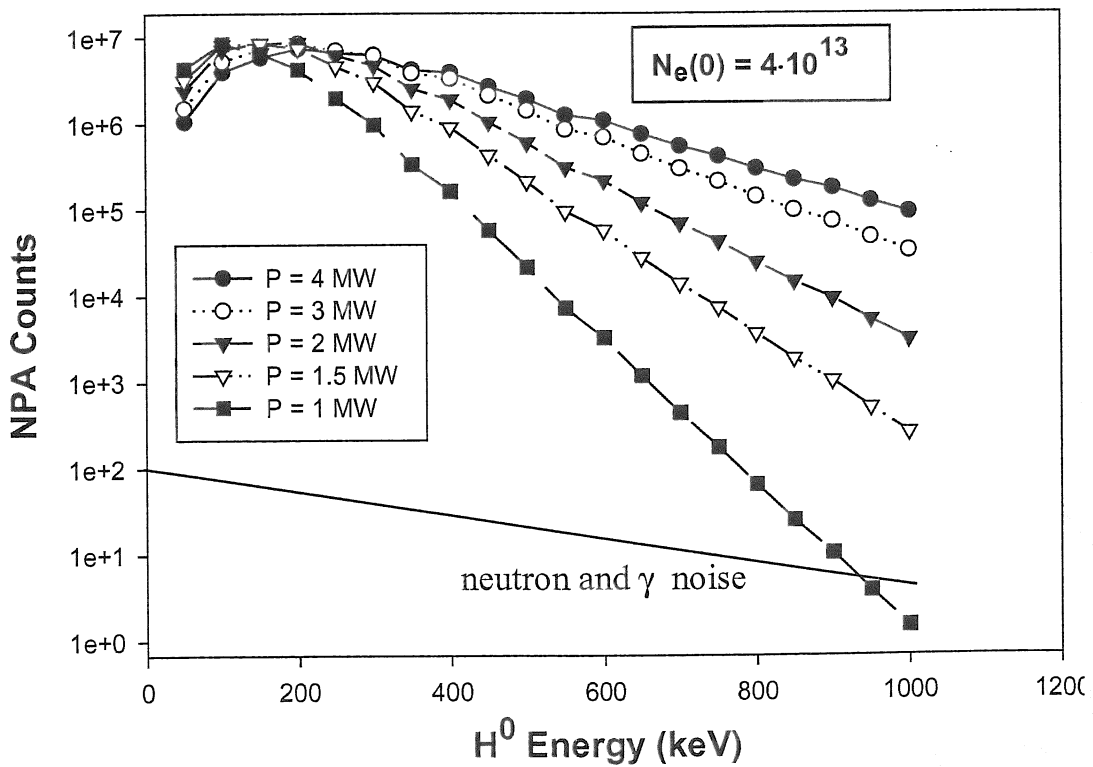
Fig. 28. Calculated NPA counts of H^0 atoms at the NPA in PCX diagnostic vs. Energy for W7-X RF minority - heated plasma (P_{RF}=6 MW) in the density range 10^{13}-$9 \cdot 10^{13}$ cm^{-3}

Fig. 29. Calculated NPA counts of H^0 at the NPA for W7-X RF minority - heated plasma for n_{e0} = $4 \cdot 10^{13}$ cm^{-3} in the range of heating power 1 – 4 MW.
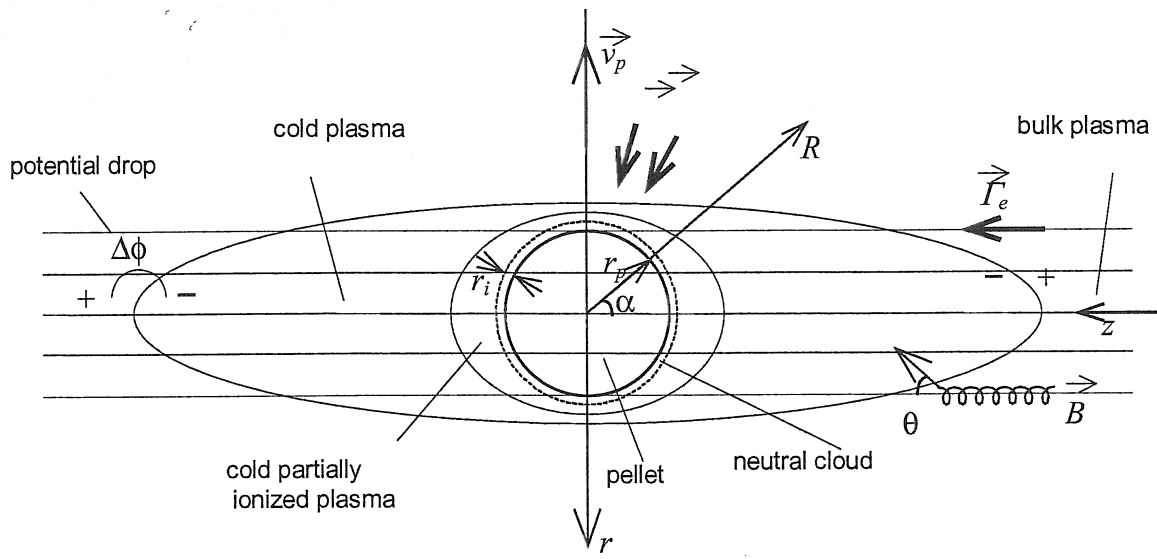
Fig. 30. The scheme of pellet-plasma interaction in charged pellet model.
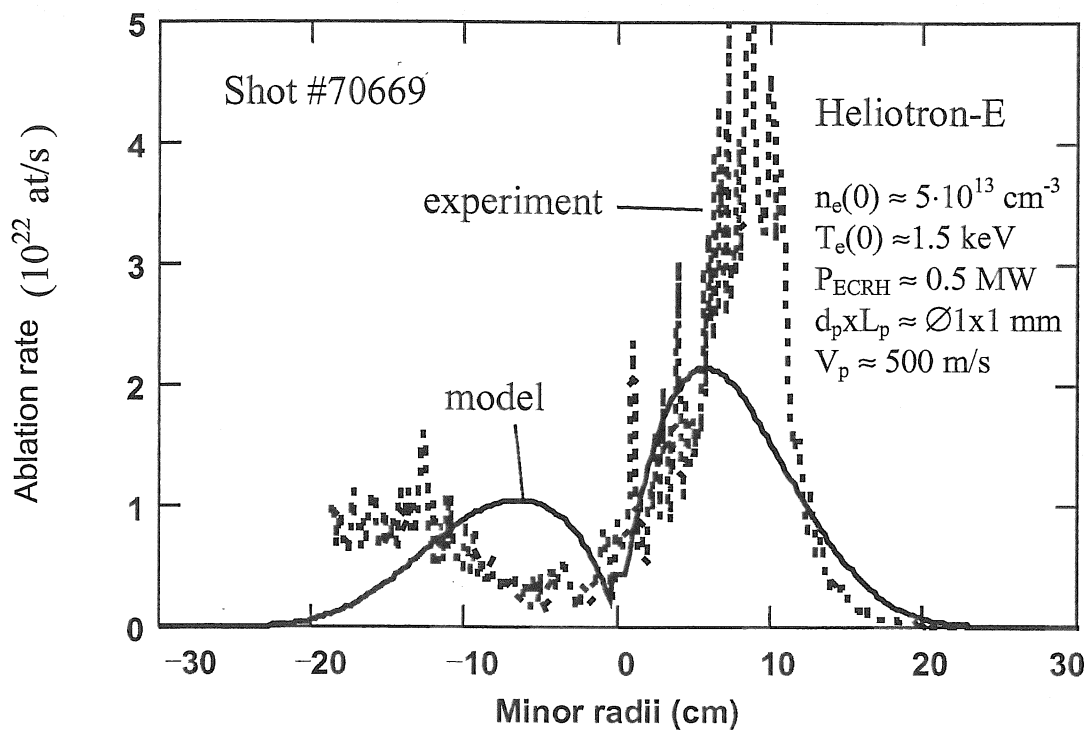
Fig. 31. Measured and simulated Li pellet ablation rate profiles
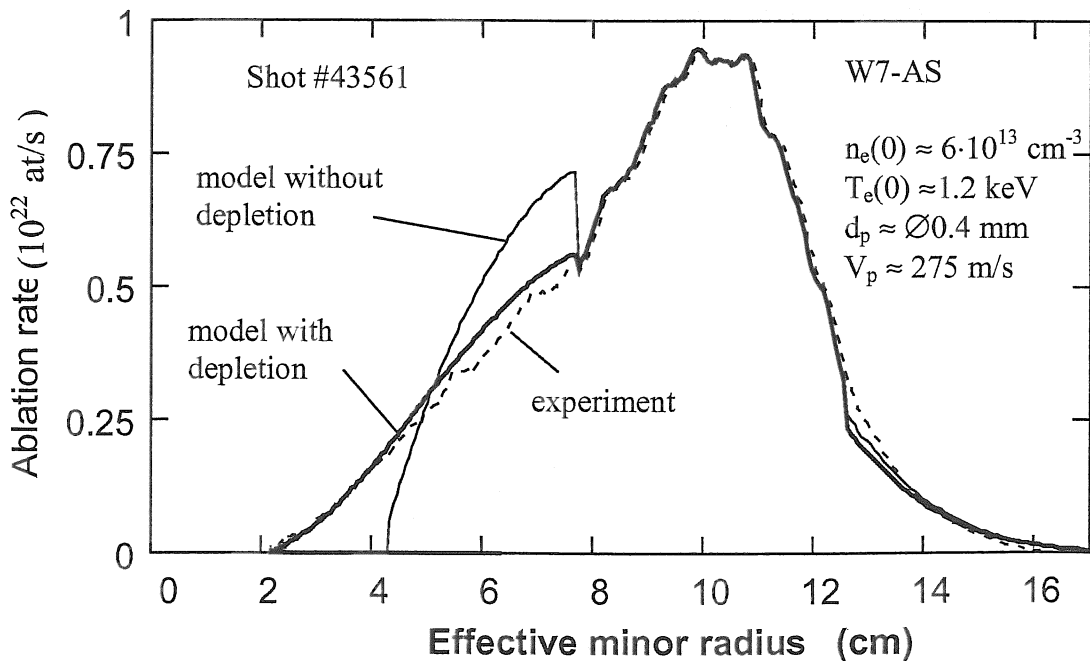in Heliotron-E ECR-heated plasma, shot #70669.

Fig. 32. Measured and simulated C pellet ablation rate profiles
in W7-AS ECR-heated plasma, shot # 43561